Draft version June 10, 2013
Preprint typeset using LaTeX style emulateapj v. 2/19/04

ABSOLUTE CALIBRATION AND CHARACTERIZATION OF THE MULTIBAND IMAGING PHOTOMETER FOR SPITZER. I. THE STELLAR CALIBRATOR SAMPLE AND THE 24 μm CALIBRATION

C. W. Engelbracht[1], M. Blaylock[1], K. Y. L. Su[1], J. Rho[2], G. H. Rieke[1], J. Muzerolle[1], D. L. Padgett[2], D. C. Hines[3], K. D. Gordon[1], D. Fadda[2], A. Noriega-Crespo[2], D. M. Kelly[1], W. B. Latter[4], J. L. Hinz[1], K. A. Misselt[1], J. E. Morrison[1], J. A. Stansberry[1], D. L. Shupe[2], S. Stolovy[2], Wm. A. Wheaton[2], E. T. Young[1], G. Neugebauer[1], S. Wachter[2], P. G. Pérez-González[1,5], D. T. Frayer[2], and F. R. Marleau[2]

Draft version June 10, 2013

ABSTRACT

We present the stellar calibrator sample and the conversion from instrumental to physical units for the 24 μm channel of the Multiband Imaging Photometer for *Spitzer* (MIPS). The primary calibrators are A stars, and the calibration factor based on those stars is 4.54×10^{-2} MJy sr^{-1} (DN/s)$^{-1}$, with a nominal uncertainty of 2%. We discuss the data-reduction procedures required to attain this accuracy; without these procdures, the calibration factor obtained using the automated pipeline at the *Spitzer* Science Center is 1.6%±0.6% lower. We extend this work to predict 24 μm flux densities for a sample of 238 stars which covers a larger range of flux densities and spectral types. We present a total of 348 measurements of 141 stars at 24 μm. This sample covers a factor of ~ 460 in 24 μm flux density, from 8.6 mJy up to 4.0 Jy. We show that the calibration is linear over that range with respect to target flux and background level. The calibration is based on observations made using 3-second exposures; a preliminary analysis shows that the calibration factor may be 1% and 2% lower for 10- and 30-second exposures, respectively. We also demonstrate that the calibration is very stable: over the course of the mission, repeated measurements of our routine calibrator, HD 159330, show a root-mean-square scatter of only 0.4%. Finally, we show that the point spread function (PSF) is well measured and allows us to calibrate extended sources accurately; Infrared Astronomy Satellite (IRAS) and MIPS measurements of a sample of nearby galaxies are identical within the uncertainties.

Subject headings: infrared: stars—instrumentation: detectors

1. INTRODUCTION

Space-based infrared astronomy satellites have used a variety of methods to perform flux calibration. For example, the Infrared Astronomy Satellite (IRAS; Beichman et al. 1988) extrapolated a ground-based 10 μm calibration out to 60 μm using stellar models and then used asteroids to transfer the 60 μm calibration to 100 μm. The Midcourse Space Experiment (MSX) was calibrated in a set of bands from $\sim 8 - 20$ μm using blackbodies ejected from the spacecraft itself (Price et al. 2004). The instruments aboard the Infrared Space Observatory (ISO) used a mix of astronomical sources, from stars for the ISO Camera (ISOCAM; Blommaert et al. 2003) to stars, asteroids, and planets for the ISO Photometer (ISOPHOT; Schulz et al. 2002) and Short Wavelength Spectrometer (SWS; Decin et al. 2000) and planets for the Long Wavelength Spectrometer (LWS; Gry et al. 2003). The Diffuse Infrared Background Experiment (DIRBE) imaged the sky in a series of bands from 1.25 μm to 240 μm and was calibrated against stars, planets, and planetary nebulae (Hauser et al. 1998). Like most of these missions, the instruments on board the *Spitzer* Space Telescope (Werner et al. 2004) are calibrated against celestial sources: for example, the Infrared Array Camera (IRAC; Fazio et al. 2004), with photometric bands from $\sim 3 - 8$ μm, is calibrated against stars (Reach et al. 2005), as is the Infrared Spectrograph (IRS; Houck et al. 2004).

The Multiband Imaging Photometer for Spitzer (MIPS; Rieke et al. 2004) has three photometric bands at 24, 70, and 160 μm. Like the other *Spitzer* instruments, the primary flux calibrators at 24 and 70 μm are stars; the calibrations are tied to the new infrared calibration by Rieke et al. (2007) and are presented here (24 μm) and in a companion paper by Gordon et al. (2007) (70 μm). The sensitivity of the 160 μm band is sufficient to allow it to be calibrated against stars, too, but a strong, short-wavelength ghost image limits the accuracy with which such hot sources can be measured; hence, an asteroid-based transfer (and the color corrections required to make the transfer) of the stellar calibration from the shorter bands (similar in spirit to the IRAS 100 μm calibration) is presented in a companion paper by Stansberry et al. (2007).

The MIPS 24 μm calibration and capabilities can be compared to several previous missions which overlap in wavelength. For example, the quoted absolute calibration uncertainties of the large surveys performed by IRAS at 25 μm, by MSX at 21 μm and by DIRBE at 25 μm are 8% (Beichman et al. 1988), 7% (Cohen et al. 2001), and 15% (Hauser et al. 1998), respectively. These missions were optimized for large area surveys and used

[1] Steward Observatory, University of Arizona, Tucson, AZ 85721; cengelbracht, mblaylock, ksu, grieke, jmuzerolle, kgordon, dkelly, jhinz, kmisselt, jmorrison, jstansberry, eyoung, gxn@as.arizona.edu
[2] Spitzer Science Center, 220-6, Caltech, Pasadena, CA 91125; rho, dlp, fadda, alberto, shupe, stolovy, waw, wachter, frayer, marleau@ipac.caltech.edu
[3] Space Science Institute, 4750 Walnut Street, Suite 205, Boulder, CO 80301; dhines@as.arizona.edu
[4] NASA Herschel Science Center, Mail Code 100-22, California Institute of Technology, 770 South Wilson Avenue, Pasadena, CA 91125; latter@ipac.caltech.edu
[5] current address: Departamento de Astrofísica, Facultad de CC. Físicas, Universidad Complutense de Madrid, E-28040 Madrid, Spain; pgperez@as.arizona.edu

older detector technology. As a result, the beam size and point source detection limits are poor compared to the *Spitzer* and ISO pointed observatories. Like MIPS, the ISOPHOT instrument was designed as a general-user instrument, but the 25 μm channel (which achieved an accuracy of $\sim$ 10%; Klaas et al. 2003) was an aperture photometer and not capable of imaging. Thus, MIPS is the first space instrument with an array detector optimized for imaging near 24 μm, achieving a point-source sensitivity of $\sim$ 60 μJy (5σ, 2000 seconds; *Spitzer* Observer's Manual), with a beam of 6″ FWHM. As we show in this paper, the absolute calibration of the MIPS 24 μm channel is accurate to 2%, which has expanded the science possible in this wavelength range. For example, the MIPS 24 μm channel allows measurement of infrared excesses around stars with lower effective temperatures and/or lower-mass debris disks than previously possible (e.g., Rieke et al. 2005; Bryden et al. 2006).

Careful data reduction procedures are essential to reproduce the results presented here; accordingly, we discuss the data reduction and photometry in some depth in § 2. The calibration factor itself is computed in § 3. To explore the quality of the calibration, we expand the sample of targets beyond those used to measure the calibration factor; the details of the flux prediction are presented in § 4. We use the expanded sample in a series of tests of the calibration, discussed in § 5. Finally, we summarize our results in §6.

2. DATA REDUCTION AND PHOTOMETRY

2.1. *Standard Processing*

The data were all obtained using the MIPS small-field photometry mode astronomical observation template (AOT). For most targets, 2 cycles of photometry using 3-second exposures were obtained, resulting in 14 individual images at each of 2 telescope nod positions (excluding the short exposure that starts the data-taking sequence at each of the two telescope nod positions). Starting with the raw data downloaded from the *Spitzer* Science Center (SSC), these data were processed using version 3.06 of the MIPS Data Analysis Tool (DAT; Gordon et al. 2005), which performs standard processing of infrared detector array data (slope fitting, dark subtraction, linearity correction, flat fielding, and mosaicking) as well as steps specific to the array used in MIPS (droop correction and dynamic range extension using the first difference frame)—these steps are described in more detail in that paper. Experience gained with the flight instrument has prompted the application of additional processing, not discussed by Gordon et al. (2005), to remove low-level instrumental artifacts. In particular, one of the four readouts on the array can incur an offset of several counts per second (due to a bright source or cosmic ray on detectors connected to that readout) relative to the other three, resulting in a striping effect (dubbed "jailbar")—an additive correction is applied to that readout to remove the effect. Also, the in-orbit flat field has several dark spots (due to particulate matter on the pick-off mirror) that shift position on the array as the scan mirror (which imposes small pointing adjustments as part of the normal observing sequence) moves. To remove these spots, a flat field specific to scan mirror position is applied as part of the standard processing. These artifacts are illustrated in Figure 1.

2.2. *Additional Processing*

There are additional low-level artifacts present in the MIPS data after the standard processing described above has been applied. We assess the severity of these effects and correct those that impact significantly our measurements. In roughly decreasing order of importance, these artifacts are:

The MIPS 24 μm array is subject to medium-term ($\sim$ 1 week) gain changes that affect pixels which have been exposed to highly saturating sources, at the level of a few percent. A typical MIPS 24 μm observation will have several regions that have been affected this way as the cumulative result of normal operations during that instrument campaign. An additional flat field, made from a median stack of the data with the source masked out, is applied to remove the gain changes.

Background levels observed by MIPS at 24 μm can change by several counts per second from image to image throughout an observing sequence, likely due to scattered zodiacal light that depends on the position of the MIPS scan mirror. Uncorrected, this can affect the photometry of our faintest ($\sim$ 10 mJy) calibrators at the level of about a percent. To mitigate this effect, we subtract the median level (after masking the source) from each image before mosaicking.

Any source that falls on the MIPS 24 μm array leaves a residual image of about 0.5% that decays with a timescale of roughly 10 seconds. The dither pattern used in the photometry AOT ensures that the source falls on a different part of the array after every exposure, and thus any residual image has decayed to a small fraction of a percent by the time the new source position is within several full-width-half-maxima of a previous position. Residual images have a negligible effect on the calibration factor we derive here, and we perform no correction for them.

Sources that saturate the MIPS 24 μm array in the full (3-second) exposures used here can affect the offset of the pixels read out after the ones on the source, and can even change the magnitude of the "jailbar" effect on those pixels, resulting in a different striping pattern above and below the source on the array. The offset is a few counts per second and only occurs for the brightest sources, so it has a negligible effect on the photometry of those sources and we make no correction here.

Examples showing the artifacts discussed here are shown in Figure 2.

2.3. *Mosaicking*

After applying the corrections discussed above, we coadd the data to make a mosaic image of each source. As the natural unit of a flat-fielded image is surface brightness, the mosaicking step conserves surface brightness as it removes optical distortions. The final images have square pixels 2.″45 on a side, very similar to the natural pixel width near the center of the array, 2.″49. The source positions in the photometry AOT range over the central 2.5′ of the array; to ensure that there are no calibration changes across the full array, we have tested the distortion correction on individual images. Using the "phot" task in the Image Reduction and Analysis Facility (IRAF[6]), we compared photometry in a fixed aperture (6

[6] IRAF is distributed by the National Optical Astronomy Observatories, which are operated by the Association of Universities

pixels in radius, with a background annulus from $7-12$ pixels) for 416 measurements of HD 042082 made during a focal plane survey which positioned the star over the full extent of the array. Without correction for distortion, the measured counts increased smoothly by 12% from the upper-left-hand corner of the array to the lower-right-hand corner of the array, inversely proportional to the 12% change in pixel area, from 6.91 square arcseconds to 6.11 square arcseconds. As expected, correcting the images for distortion eliminates this trend, resulting in a 1σ dispersion in the measurements of only 0.8%.

2.4. *Photometry*

To compute aperture corrections for photometry, we make use of a point response function (PRF) constructed as follows. We start with a point spread function (PSF) of a 10000 K blackbody (the spectral energy distributions of the stars we use to calibrate differ negligibly from this at 24 μm) generated using the Spitzer TinyTim software (STinyTim; Krist 2002). The PSF is computed at the center of the array using an image size ($10'$ width) large enough to encompass $> 99\%$ of the light. We "observe" the model using the MIPS simulator (software designed to simulate MIPS data, including optical distortions, using the same observing templates used in flight) and mosaic the simulated data using the same software with which we processed the real data. We compare the result to one of the calibration stars in Figure 3. The structure predicted by the model, down to very faint levels and in the diffraction spikes, is very similar to what is observed on a real star. Additional insight is gained from a comparison of radial profiles (Figure 4), where it can be seen that the model is an excellent description of the data, out to the third Airy ring. A similar, and slightly improved, fit to the radial profile can be obtained by smoothing the STinyTim model by the equivalent of a boxcar 1.8 pixels in width (possibly indicating a small amount of pointing jitter or scattered light, neither of which is modeled by the simulator). We apply the "phot" task in IRAF to the boxcar-smoothed image to compute the aperture corrections, representative values of which are shown in Table 1. We find that the counts measured by various photometry routines vary by about a percent, so we assign a 1% uncertainty to the aperture correction.

We perform aperture photometry on the observations using an aperture $35''$ in radius, with a background annulus from $40''$ to $50''$ in radius. This aperture is large enough to minimize uncertainties due to centroiding errors, and to ensure that any uncertainties in the aperture correction have a small effect on the derived counts. We derive the uncertainty on each measurement from the scatter of the pixel values in the background aperture. The measurements are listed in Table 2.

2.5. *Comparison to SSC Pipeline*

We compare the measurements made on data reduced using the DAT to those obtained using identical photometry procedures on data processed using the automated pipeline at the SSC, which does not apply the second flat field (made using a median stack of the data; see § 2.2) or the background subtraction. We convert the units of the SSC data products from MJy/sr to DN/s by dividing by the FLUXCONV value found in the header. Based on 90 measurements of HD 159330 processed using the S15.3.0 version of the pipeline, we find that the count rate in the pipeline-reduced data is $1.6\% \pm 0.6\%$ higher than in data reduced using the DAT. The difference between the reductions is marginally significant (2.7σ) and may be due to the extra processing steps applied to the DAT-processed data.

2.6. *Scan Map Calibration*

The results we present here rely on measurements of calibrator stars performed using the photometry AOT, which images the sky in a nod-and-stare pattern. MIPS has a second imaging mode, the scan map AOT, which images the sky using a continuous track of the spacecraft. The scan mode uses the same optical train as the photometry mode and so we expect that the calibration derived here would apply equally to both modes. To check whether subtle differences exist in the shape of the PSF that might affect the calibration, we compare photometry in scan and photometry modes on two stars observed in multiple epochs, HD 159330 and HD 163588. We find that the radial profiles in scan and photometry modes are identical within the uncertainties and that photometry in these two modes agrees within $\sim 1\%$, confirming that the photometry calibration is applicable to scan-mode data. Similar results were found by Fadda et al. (2006).

3. THE 24 μm CALIBRATION FACTOR

Following Rieke et al. (2007), we base the flux calibration of the MIPS 24 μm band on A stars. We adopt the sample of 22 A stars from Rieke et al. (2007), as a consistent suite of measurements is available for these targets and the sample has already been vetted for sources which would bias the calibration, such as those with an infrared excess. Here and throughout this work, monochromatic flux densities are computed at 23.675 μm, the effective wavelength of the 24 μm band, although we will continue to use the shorthand "24 μm" for convenience. We compute 24 μm flux densities using the extinction-corrected K_s magnitudes computed by Rieke et al. (2007), a $K_s - [24]$ color difference of 0 magnitudes, and the 24 μm (i.e., 23.675 μm) zero point derived by Rieke et al. (2007), 7.17 Jy. We apply the aperture correction derived in § 2 (1.08) to the measurements from Table 2, averaging multiple measurements when available. The counts in that table are integrations over an aperture, so we convert the implied unit of "pixel" (that we have ignored thus far) to an angular area using the pixel size ($2\farcs45$ on a side) of our mosaics. The calibration factor is the weighted average of the ratio of the 24 μm predictions to the observed count rate, or 4.54×10^{-2} MJy sr^{-1} (DN/s)$^{-1}$, with a formal uncertainty of 0.7%. At the pixel scale of our mosaics, this factor is equivalent to 6.40×10^{-6} Jy pixel^{-1} (DN/s)$^{-1}$ (which can be converted to other pixels scales by multiplying by the square of the ratio of the pixel size to $2\farcs45$). Following Rieke et al. (2007), we assign an uncertainty of 2% to the calibration factor to allow for systematic effects in propagating the near-infrared measurements to 24 μm. Where care is taken to apply the corrections discussed in § 2 and to treat calibration stars and other targets in a consistent manner, this calibration accuracy

for Research in Astronomy, Inc., under cooperative agreement with the National Science Foundation.

can be maintained in science data. The data used to compute the calibration factor are summarized in Table 3.

The calibration factor was derived using stars, and no color corrections were applied to the measurements used here. Stars are relatively blue ($f_\nu \propto \nu^{-2}$) at MIPS wavelengths, so color corrections are required to calibrate sources with different spectral distributions. As shown by Stansberry et al. (2007), however, these corrections are small in the MIPS 24 μm band: they are no more than 3% over a range of power-law indices (-3 to 3) and do not exceed 5% for blackbody sources above a temperature of 57 K.

4. SAMPLE AND PREDICTED FLUXES

The sample of stars used in § 3 to derive the 24 μm calibration factor covers a limited dynamic range and is too small to probe statistically characteristics of the instrument behavior such as linearity and the effects of sky brightness. Furthermore, these stars are too faint to be useful as calibrators for the MIPS 70 μm band (discussed by Gordon et al. 2007). In this section, we develop an expanded sample of 24 μm calibrators to support our characterization of the performance of the instrument, which we discuss in § 5. These stars were selected to explore the dynamic range of the instrument within reasonable integration times and to probe the effects of spectral type and environment (primarily foreground/background level) on the calibration.

4.1. *Zero-point Conversions for Additional Data Sets*

We predict flux densities at 24 μm for the expanded MIPS calibration target list by extrapolating measurements made at near- and mid-infrared wavelengths. The scale factors for the 2MASS (Skrutskie et al. 2006) measurements of A and G stars made in the read-1 (the 51 ms exposure used to measure sources that saturate the full 1.3 s exposure) data are given by Rieke et al. (2007), who find $K_s-[24]$ is 0 (by definition) and 0.045 ± 0.011 magnitudes, respectively. The 2MASS read-1 magnitude limit (~ 3.5 magnitudes at K_s) is not low enough to constrain measurements throughout the MIPS dynamic range, so we must incorporate additional data sets into our flux predictions for the bright 24 μm calibrators. We discuss here the validation of additional data sets and derive the scale factors required to put them on the same system as the 2MASS read-1 measurements (and therefore the same system as the MIPS 24 μm measurements), allowing direct comparison to the results of Rieke et al. (2007).

4.1.1. *2MASS Saturated-Source Magnitudes*

Below magnitudes of $\sim$ 4.5, 4, and 3.5 at J, H, and K_s, respectively, 2MASS data are saturated even in the read-1 measurements used to constrain the calibration factor derived in § 3. Measurements for saturated sources are reported by the 2MASS project and are obtained by fitting to the radial profiles of the unsaturated portion of the stellar image, but large uncertainties 20%−30% are associated with these measurements. To reduce the uncertainties associated with using the saturated 2MASS magnitudes, we compute the offset between the saturated and read-1 magnitudes.

Kimeswenger (2005) presents photometry in the J and K_s bands for a sample of $\sim$ 600 stars that overlaps the 2MASS read-1 and saturated-source magnitude ranges. This bright-star survey uses the same camera as the Deep Near-Infrared Survey of the Southern Sky (DENIS) with the addition of neutral-density filters, so we apply the DENIS transformations computed by Carpenter (2001) to put the magnitudes on the 2MASS system. (This step isn't strictly necessary since, as we discuss below, we are using these measurements differentially.) We compare the 2MASS measurements to those by Kimeswenger (2005) over different magnitude ranges to determine the offset between the 2MASS read-1 and saturated-source magnitudes. At faint levels (well above the limits quoted above, to ensure that read-1 measurements were not affected by any saturated sources), the 2MASS and the transformed Kimeswenger (2005) magnitudes are in excellent agreement: the weighted average (rejecting points more than 3σ from the median) of $J(2MASS) - J(Kimeswenger)$ between magnitudes 8.5 and 5.6 is 0.001 ± 0.002 magnitudes, and $K_s(2MASS) - K_s(Kimeswenger)$ between magnitudes 7.5 and 4.2 is 0.023 ± 0.003 magnitudes. Below those magnitude limits, the offsets are $J(2MASS) - J(Kimeswenger) = 0.053 \pm 0.005$ magnitudes and $K_s(2MASS) - K_s(Kimeswenger) = 0.058 \pm 0.008$ magnitudes. The difference between the faint J magnitudes is not significant, but we do include the difference between the faint K_s magnitudes in computing offsets ($m_{read-1} - m_{saturated}$) of -0.053 magnitudes at J and -0.035 magnitudes at K_s. These offsets are added to saturated 2MASS magnitudes to put them on the read-1 scale. To further reduce the uncertainty, we average the J and K_s magnitudes to compute a "super"-K_s magnitude, after correcting J to K_s using the $J-K$ colors (after correcting the colors to the 2MASS system using the transformations computed by Carpenter 2001) of stars tabulated by Tokunaga (2000).

4.1.2. *Johnson Photometry*

Johnson et al. (1966) measured $\sim$ 650 bright stars in the J and K bands. This sample is large, homogeneously observed, and the measurements have significantly smaller uncertainties than the saturated sources observed by 2MASS. For example, the star HD 001013 was observed 91 times by Johnson et al. (1966). After applying an airmass correction derived from the data, we find a root-mean-square (RMS) deviation of 0.037 magnitudes in these measurements. We conservatively assign a 1σ uncertainty of 0.04 magnitudes to the photometry by Johnson et al. (1966).

To compute the offset between the Johnson et al. (1966) magnitudes and 2MASS, we transform the measurements to the 2MASS system using the equations derived by Carpenter (2001) for the Koornneef (1983) system, which is most similar to the system used by Johnson et al. (1966). The weighted average (rejecting points more than 3σ from the median) of $J(2MASS) - J(transformed\ Johnson)$ is 0.028 ± 0.007 magnitudes and $K_s(2MASS) - K(transformed\ Johnson)$ is 0.004 ± 0.005 magnitudes. The offset in the K_s band is not significant, but we apply a correction of 0.028 magnitudes to the measurements at J. In addition, since all the MIPS calibrators that were also measured by Johnson et al. (1966) are well into the saturated 2MASS range, we apply the same offsets applied to the saturated 2MASS measurements, for net corrections of -0.025 magnitudes

at J and -0.035 magnitudes at K_s (plus the color transformation from Johnson to 2MASS). Finally, we combine the J and K_s data to form super-K_s as for the 2MASS data.

4.1.3. *IRAS Measurements*

Many of the bright MIPS calibrators were detected by IRAS at 12 and 25 μm. The MIPS 24 μm band was demonstrated by Rieke et al. (2007) to be linear within $\sim 1\%$ below 1 Jy, so we can use the overlap between MIPS and IRAS measurements in this flux range to constrain the linearity of IRAS and probe for effects of molecular absorptions in the 12 μm band. To ensure that the IRAS measurements are on the same scale as the other photometry we use to predict flux densities for our calibrators, we empirically derive the ratio between the IRAS bands and the MIPS 24 μm band below 1 Jy for the calibrator stars, then apply this result over the full range of calibrator fluxes.

We obtain IRAS measurements of the MIPS calibrators from the faint source catalog (FSC; used because the improved sensitivity relative to the point source catalog provides more overlap with the MIPS sample), using only high-quality (quality flag "3") measurements. We applied color corrections appropriate to the temperature of each star to these observations and also applied the corrections measured by Rieke et al. (2007): 0.992 at 12 μm and 0.980 at 25 μm. The ratio of the MIPS 24 μm measurement to the IRAS measurement, normalized to the average ratio, is plotted in Figure 5. The scatter in the measurements becomes obviously larger near the IRAS detection limit, around the equivalent 24 μm flux density of 60 and 80 mJy at 12 and 25 μm, respectively. The slope of the ratio as a function of brightness above these limits is consistent with 0 for both bands, indicating they are linear in this brightness range. The average value of $f_\nu(24\ \mu\mathrm{m})/f_\nu(12\ \mu\mathrm{m})$ is 0.265 while $f_\nu(24\ \mu\mathrm{m})/f_\nu(25\ \mu\mathrm{m})$ is 1.11. Both values are very similar to the values derived from Kurucz (1993) models of these stars, 0.266 and 1.11, respectively. As shown in Figure 6, $f_\nu(24\ \mu\mathrm{m})/f_\nu(12\ \mu\mathrm{m})$ has a mild dependence on temperature (possibly the result of molecular absorptions in the 12 μm band becoming important in cool stars), so the ratio is better described as $0.276 - 1.94 \times 10^{-6} * T_{eff}[K]$. No significant trend with temperature is detected at 25 μm.

The factors we derive in this section to convert the zero points of saturated 2MASS magnitudes, Johnson et al. (1966) magnitudes, and IRAS 12 μm and 25 μm measurements to the system used by MIPS are summarized in Table 4.

4.2. *The Calibration of Cool Stars*

We compute an average super-$K_s - [24]$ (by applying the aperture correction, 1.08, derived in § 2.4 and the calibration factor derived in § 3 to the measurements in Table 2) color for the cool (K and M giants) stars in our sample, which can be compared directly to the A and G star color computed by Rieke et al. (2007), modulo any offset (typically a fraction of a percent) between super-K_s and K_s. The weighted average color of the K and M stars in our sample (after rejecting points greater than 3σ from the mean) is 0.104 ± 0.006 magnitudes.

4.3. *Predictions*

We list the photometry used to constrain the flux density predictions, after applying the corrections detailed above, in Table 5. The 24 μm flux densities for each source are the weighted average of the predictions derived from the entries in that table. We also list the predicted flux densities and their uncertainties in Table 5. We note that the predictions can be slightly different than those implicit in Table 3, since we used super-K_s in Table 5 and K_s was used in Table 3, although the average difference is insignificant: 0.002 ± 0.005 magnitudes. We also include predicted background levels, computed using the *Spitzer* Planning Observations Tool[7] (SPOT); the background listed is the average of the range when the target is visible, and the uncertainty is half the difference between the extreme values.

5. CHECKS ON THE 24 μm CALIBRATION

In this section, we perform various checks on the 24 μm calibration, such as repeatability, linearity, and the effects of spectral type, exposure time, and background. Except for the repeatability check, we compute a single calibration factor for each star by dividing the prediction (Table 5) by the pixel area and the weighted average of all measurements of the count rate for each star (Table 6). The calibration factors derived from some stars differ from the adopted calibration factor by more than 5σ—these stars were not used in the checks below. As shown in Table 7, most of the rejected stars show infrared fluxes above the predictions (i.e., the calibration factor is low).

5.1. *Repeatability*

The primary routine calibrator for the MIPS 24 μm channel is HD 159330, a K2III star near the *Spitzer* continuous viewing zone (CVZ). When visible, this star is observed each time the instrument is turned on, to monitor photometric stability and check for changes in the calibration. A second routine calibrator, the K0III star HD 173398, is also monitored to fill in the gaps when HD 159330 is not visible. We plot 100 measurements of HD 159330 and 46 measurements of HD 173398 in Figure 7. The RMS scatter in the HD 159330 measurements is 0.4% (compared to 0.7% in the SSC-pipeline-reduced data discussed in § 2.5), while the scatter in the HD 173398 measurements is 0.5%. A gradual reduction in the instrument response of $\sim 0.5\%$ over the first 300 days is apparent in the data and is the cause of some of the scatter computed for HD 159330. As this trend is insignificant compared to the uncertainty on the absolute calibration (cf. § 3), we have not attempted to correct it.

5.2. *Linearity*

We check for effects of flux nonlinearity in the calibration by comparing calibration factors over a range of 460 in source brightness. We plot the calibration factors in Figure 8. We find no significant trend of calibration factor with source brightness—a least-squares fit to the data shows a difference of only 0.3% between 9 mJy and 4 Jy. The observed scatter of calibration factors is larger than

[7] http://ssc.spitzer.caltech.edu/propkit/spot/

can be explained by the error bars. The unaccounted-for scatter in the calibration factors is likely due to systematic uncertainties on the flux predictions for the individual stars, possibly from variability or small infrared excesses.

5.3. *Spectral Type*

As discussed in §4, we have derived calibration factors using 3 broad types of stars (hot dwarfs, solar analogs, and cool giants) to look for systematic effects with stellar temperature. The weighted average calibration factor of each broad spectral type is 4.49×10^{-2}, 4.62×10^{-2}, and 4.49×10^{-2} MJy/sr/(DN/s) for 32 A, 37 G, and 25 K/M stars, respectively. These values are all consistent with the adopted calibration factor within the uncertainty (deviating by -1.1%, 1.8%, and -1.1%, respectively), but the differences may reflect real uncertainties in the colors of different types of stars and in our treatment of saturated 2MASS magnitudes.

5.4. *Exposure Time*

A small subset of the calibrators (11 stars) was measured using 10- and 30-second exposures in addition to the 3-second exposures—the weighted average counts per second from these stars is 1% and 2% higher using 10- and 30-second exposures, respectively. We find that the residual images in the 10- and 30-second exposures are roughly twice as bright as in the 3-second exposures, so it is likely that the excess is due to buildup of residual charge during the longer exposures.

5.5. *Background*

In general, astronomical sources of interest at 24 μm will be observed against a wide range of background levels, so we examine whether the derived calibration factor depends on background. Such an effect might be expected due to background light scattering onto the detector or due to systematic effects on the droop correction. We find no significant effect on the calibration over a factor of $\sim$ 5 in background, as shown in Figure 9. A least-squares fit to the data indicates a slope of only marginal significance: $5.4 \times 10^{-4} \pm 2.9 \times 10^{-4}$ MJy/sr/(DN/s) / MJy/sr.

5.6. *Comparison to Another Infrared Calibration*

As discussed in detail by Rieke et al. (2007) and cited in § 4.1.3, the calibration presented here is based on an updated calibration system which is offset by a small ($\sim 2-3\%$) amount from other infrared calibrations commonly in use. For the convenience of the reader, we present a direct comparison of our measurements to predictions in one of those systems, that prepared by Cohen and collaborators. Specifically, we compute predicted flux densities at 24 μm for the 10 "template" stars (Cohen et al. 1999, and references therein) observed by us by interpolating the values given by the templates. We adopt the model uncertainties provided by the templates. We take the "observed" values and uncertainties from Table 6 and convert them to flux densities using the calibration factor computed in § 3. We present the data used for and the results of this comparison in Table 8, where we reject the star HD020722 due to a contaminating background source at 24 μm (cf. Table 7). The weighted average ratio of our measurements to the predictions is 1.026 ± 0.013, i.e., measurements on the Cohen et al. (1999) system can be converted to the system used by MIPS by multiplying by this factor. Much of this difference is due to the different fluxes adopted for Vega at 10.6 μm (35.03 Jy by Rieke et al. (2007) and 34.38 Jy by Cohen et al. (1999), which differ by 2%).

5.7. *Extended-Source Calibration*

As demonstrated in § 2, the model PSF is a good match to the data out to large radii, so we expect the extrapolation of the calibration to infinite radii to be well understood. As a check, we compare measurements of extended sources (nearby galaxies) observed by the *Spitzer* legacy teams SINGS (*Spitzer* Infrared Nearby Galaxies Survey; Kennicutt et al. 2003) and SAGE (Surveying the Agents of a Galaxy's Evolution; Meixner et al. 2006) and by guaranteed time observers (Hinz et al. 2004; Gordon et al. 2006a,b) to IRAS measurements. We apply color corrections from Beichman et al. (1988) (IRAS) and Stansberry et al. (2007) (MIPS) assuming a power-law spectrum fit to the 12/25 μm or 24/70 μm data to the IRAS and MIPS (SINGS measurements taken from Dale et al. 2007) measurements, and also correct the MIPS measurements to the calibration factor derived in § 3. We interpolate the IRAS 12 μm and 25 μm measurements to the effective wavelength of the 24 μm band, 23.675 μm. We compare the results graphically in Figure 10. The weighted average ratio of MIPS to IRAS measurements is 0.96, well within the 8% combined uncertainty of both instruments.

6. SUMMARY

We discuss the flux calibration of the MIPS 24 μm band, which is based on stars. We describe the data reduction and photometric procedures we use for the calibration sources, which produce fluxes that are $1.6 \pm 0.6\%$ lower than those achieved by the automated pipeline at the *Spitzer* Science Center. We show that the calibration of the two imaging modes, photometry and scan map, is consistent within 1%.

We compute the calibration factor (the conversion from count rate to physical units) for the MIPS 24 μm band, using a sample of 22 A stars that has been well measured and has been carefully vetted to exclude debris-disk systems. We find a value of 4.54×10^{-2} MJy sr^{-1} (DN/s)$^{-1}$, with an uncertainty of 2%. Based on this uncertainty and the difference between the SSC pipeline and the DAT discussed in § 2.5 and summarized above, we recommend that a net uncertainty on the calibration of 4% is appropriate for general use.

We present a sample of 238 stars appropriate for use as MIPS flux calibrators. We have computed flux densities of these stars at the effective wavelength of the 24 μm band, 23.675 μm. We present 348 measurements of 141 of these stars, and combine those measurements with the 24 μm predictions to test various aspects of the calibration. We find that routine monitoring of a star near the *Spitzer* constant viewing zone demonstrates that 24 μm photometry with MIPS is repeatable to 0.4%. The calibration is linear to 0.3% over a range of $\sim$ 460 in flux density, and there are no significant systematic effects on the calibration due to spectral type, background, or angular extent of the source.

We thank John Carpenter for helpful discussions, especially regarding the effect of exposure time on the measured count rate. We would also like to thank the anonymous referee, whose comments improved this paper. This work is based on observations made with the *Spitzer Space Telescope*, which is operated by the Jet Propulsion Laboratory, California Institute of Technology under NASA contract 1407. This research has made use of the SIMBAD database, operated at CDS, Strasbourg, France. This publication makes use of data products from the Two Micron All Sky Survey, which is a joint project of the University of Massachusetts and the Infrared Processing and Analysis Center/California Institute of Technology, funded by the National Aeronautics and Space Administration and the National Science Foundation. Support for this work was provided by NASA through Contract Number #1255094 issued by JPL/Caltech.

REFERENCES

Beichman, C. A., Neugebauer, G., Habing, H. J., Clegg, P. E., & Chester, T. J. 1988, Infrared astronomical satellite (IRAS) catalogs and atlases. Volume 1: Explanatory supplement
Blommaert, J. A. D. L., et al. The ISO Handbook, Volume II - CAM - The ISO Camera
Bryden, G., et al. 2006, ApJ, 636, 1098
Carpenter, J. M. 2001, AJ, 121, 2851
Cohen, M., Walker, R. G., Carter, B., Hammersley, P., Kidger, M., & Noguchi, K. 1999, AJ, 117, 1864
Cohen, M., Walker, R. G., Jayaraman, S., Barker, E., & Price, S. D. 2001, AJ, 121, 1180
Dale, D. A., et al. 2007, ApJ, 655, 863
Decin, L., Waelkens, C., Eriksson, K., Gustafsson, B., Plez, B., Sauval, A. J., Van Assche, W., & Vandenbussche, B. 2000, A&A, 364, 137
Fadda, D., et al. 2006, AJ, 131, 2859
Fazio, G. G., et al. 2004, ApJS, 154, 10
Gordon, K. D., et al. 2005, PASP, 117, 503
Gordon, K. D., et al. 2006a, ApJ, 638, L87
Gordon, K. D., Engelbracht, C. W., Smith, J.-D. T., Rieke, G. H., & Misselt, K. A. 2006b, astro-ph/0605544
Gordon, K. D., et al. 2007, submitted to PASP
Gry, C., et al. The ISO Handbook, Volume III - LWS - The Long Wavelength Spectrometer
Hauser, M. G., Kelsall, T., Leisawitz, D., & Weiland, J. 1998, COBE Diffuse Infrared Background Experiment (DIRBE) Explanatory Supplement
Hinz, J. L., et al. 2004, ApJS, 154, 259
Houck, J. R., et al. 2004, ApJS, 154, 18
Johnson, H. L., Iriarte, B., Mitchell, R. I., & Wisniewskj, W. Z. 1966, Communications of the Lunar and Planetary Laboratory, 4, 99
Kennicutt, R. C., Jr., et al. 2003, PASP, 115, 928
Kimeswenger, S. 2005, High Resolution Infrared Spectroscopy in Astronomy, 411
Klaas, U., et al. 2003, ESA SP-481: The Calibration Legacy of the ISO Mission, 19
Koornneef, J. 1983, A&AS, 51, 489
Krist, J. 2002, Tiny Tim/SIRTF User's Guide (Pasadena: SSC)
Meixner, M., et. al. 2006, astro-ph/0606356
Price, S. D., Paxson, C., Engelke, C., & Murdock, T. L. 2004, AJ, 128, 889
Reach, W. T., et al. 2005, PASP, 117, 978
Rieke, G. H., et al. 2004, ApJS, 154, 25
Rieke, G. H., et al. 2005, ApJ, 620, 1010
Rieke, G. H., et al. 2007, in preparation
Schulz, B., et al. 2002, A&A, 381, 1110
Skrutskie, M. F., et al. 2006, AJ, 131, 1163
Stansberry, J. A., et al. 2007, submitted to PASP
Su, K. Y. L., et al. 2006, ApJ, in press
Tokunaga, A. T. 2000, in Allen's Astrophysical Quantities, 4th edition, ed. A. N. Cox, Springer-Verlag: NY, p. 143
Werner, M. W., et al. 2004, ApJS, 154, 1

TABLE 1
24 μM Aperture Correction Factors for a 10,000 K Blackbody.[a]

description	radius	background annulus 6-8	7-13	20-32	40-50	none
half first dark ring	3.5	2.78	2.80	2.57	2.56	2.56
center of first dark ring	7.0	···	2.05	1.61	1.61	1.61
outside first bright ring	13.0	···	···	1.17	1.16	1.16
center of second dark ring	20.0	···	···	1.15	1.13	1.12
outside second bright ring	35.0	···	···	···	1.08[b]	1.06

[a]All radii are measured in arcseconds.
[b]Aperture correction used for calibration.

TABLE 2
24 μm Measurements of MIPS flux calibrators.

Name	days since mission start	AORKEY[a]	DCE[b] time (s)	count rate (DN/s)	uncertainty (DN/s)
BD+621644	496.4	13071616	3	1.033e+04	5.19e+01
HD000319	300.4	3972864	3	6.708e+03	5.00e+01
HD001160	322.3	10090496	3	1.395e+03	1.56e+01
HD001644	322.3	10090752	3	8.191e+03	5.69e+01
HD002151	806.5	16276992	3	3.271e+05	1.23e+03
HD002811	298.4	9940224	3	1.591e+03	3.35e+01
HD008941	359.7	5414400	3	7.202e+03	3.46e+01
HD009927	871.5	16619776	3	6.045e+05	2.45e+03
HD011413	298.5	3973376	3	7.866e+03	3.87e+01
HD014943	298.4	9940480	3	7.180e+03	2.84e+01
HD015008	69.4	7345408	3	2.698e+04	1.14e+02
	84.0	7979264	3	2.662e+04	1.09e+02
	1133.7	20460800	3	2.672e+04	5.28e+01
	1133.6	20461056	30	2.730e+04	1.51e+01
	1133.7	20461312	10	2.705e+04	2.31e+01
HD015646	394.6	3973888	3	2.997e+03	4.84e+01
HD017254	339.7	11783424	3	4.482e+03	2.75e+01
	466.2	12871936	3	4.578e+03	2.81e+01
	1133.6	20462848	3	4.649e+03	5.28e+01
	1133.6	20463104	10	4.575e+03	2.31e+01
	1133.6	20463360	30	4.689e+03	1.44e+01
HD019019	367.9	5407744	3	6.204e+03	3.74e+01
HD020722	386.5	12063488	3	5.818e+03	4.56e+01
HD020888	339.7	11783680	3	5.624e+03	2.99e+01
	630.9	13613568	3	5.427e+03	2.79e+01
HD020902	905.8	16868864	3	6.872e+05	2.62e+03
HD021981	153.6	8812544	10	6.089e+03	1.33e+01
HD025860	702.7	15421440	3	4.202e+03	3.26e+01
HD027466	392.1	5412096	3	3.146e+03	3.18e+01
HD028099	762.9	15991808	3	2.546e+03	2.80e+01
HD028471	181.1	9059072	10	3.173e+03	1.81e+01
HD029461	762.9	15992064	3	2.759e+03	2.77e+01
HD030246	762.9	15992320	3	2.497e+03	2.75e+01
HD032831	386.4	12062464	3	2.301e+05	8.06e+02
HD034868	179.9	3983360	3	3.851e+03	3.89e+01
HD035666	364.2	11891968	3	3.416e+04	1.34e+02
HD036167	920.0	16869120	3	5.627e+05	2.23e+03
HD037962	414.8	5412864	3	3.281e+03	3.12e+01
HD038949	416.4	5340160	3	2.871e+03	3.10e+01
HD039608	61.0	7200768	3	3.844e+04	1.49e+02
	69.9	7743232	3	3.832e+04	1.46e+02
	84.0	7977472	3	3.805e+04	1.43e+02
	1133.7	20460032	3	3.780e+04	5.19e+01
	1133.7	20460288	10	3.842e+04	2.38e+01
	1133.7	20460544	30	3.878e+04	1.56e+01
HD040129	386.5	12062720	3	2.025e+03	2.04e+01
HD040335	202.7	9192192	3	2.866e+03	3.25e+01
HD041371	386.5	12062976	3	1.491e+04	7.41e+01
	1133.7	20461568	10	1.494e+04	2.29e+01
	1133.7	20461824	30	1.502e+04	1.42e+01
	1133.7	20463616	3	1.462e+04	5.06e+01
HD042525	631.5	13588224	3	5.116e+03	2.85e+01
HD042701	35.3	6772992	3	4.363e+04	1.79e+02
	228.2	9457920	3	4.333e+04	1.61e+02
HD043107	34.1	6765056	3	7.581e+03	1.05e+02
	34.1	6765312	10	7.757e+03	7.84e+01
	34.1	6765568	30	8.214e+03	7.31e+01
	34.1	6765824	3	8.087e+03	6.96e+01
	69.5	7342080	3	8.176e+03	6.96e+01
	69.5	7342336	10	8.386e+03	5.52e+01
	69.5	7344640	3	8.373e+03	1.64e+01
	69.5	7344896	3	8.104e+03	2.50e+01
	69.2	7346944	3	8.090e+03	6.99e+01
	69.3	7347200	3	7.298e+04	3.53e+02
	69.3	7347968	3	8.048e+03	6.92e+01
	91.8	7866112	3	8.122e+03	6.60e+01
	91.8	7866368	3	7.984e+04	4.24e+02
	91.8	7867136	3	8.206e+03	6.32e+01
HD044594	70.6	7339008	3	9.411e+03	4.79e+01
HD045557	631.5	13588480	3	5.492e+03	3.51e+01
HD046190	258.0	9662976	3	3.703e+03	2.82e+01
HD046819	393.7	12063232	3	8.504e+03	4.94e+01
HD047332	364.2	11892224	3	2.595e+03	2.60e+01
HD050310	205.7	9192448	3	7.865e+05	2.88e+03

TABLE 2 — *Continued*

Name	days since mission start	AORKEY[a]	DCE[b] time (s)	count rate (DN/s)	uncertainty (DN/s)
HD053501	35.3	6773248	3	1.837e+05	6.89e+02
	60.9	7199232	3	1.840e+05	6.66e+02
	69.9	7742976	3	1.840e+05	7.02e+02
	84.0	7977728	3	1.831e+05	1.06e+03
HD057336	631.5	13588736	3	1.403e+03	3.44e+01
HD058142	49.7	7145472	3	1.458e+04	1.33e+02
HD060178	228.2	9458176	3	2.584e+05	7.17e+02
HD061929	631.5	13588992	3	3.038e+03	2.66e+01
HD064324	416.9	5400832	3	3.672e+03	3.87e+01
HD065517	631.6	13589248	3	2.122e+03	1.81e+01
HD066751	416.2	5409280	3	9.671e+03	2.80e+01
HD069863	631.5	13589504	3	1.240e+04	5.52e+01
HD073210	226.2	3986432	3	3.707e+03	5.55e+01
HD073666	227.7	3986688	3	2.541e+03	5.66e+01
HD073819	226.2	3987200	3	3.170e+03	5.29e+01
HD077281	627.2	13589760	3	1.673e+03	1.99e+01
HD080007	319.4	10091008	3	2.592e+05	9.55e+02
	339.8	11783936	3	2.596e+05	9.23e+02
HD082308	97.0	7973888	3	7.022e+05	2.59e+03
HD082621	70.6	7338496	3	1.909e+04	8.24e+01
HD087901	96.9	7972096	3	2.350e+05	7.87e+02
HD091375	258.0	9663232	3	1.602e+04	6.73e+01
HD092788	494.8	5440512	3	5.299e+03	3.93e+01
HD092845	301.2	3990016	3	7.166e+03	4.51e+01
HD096833	97.0	7974144	3	7.470e+05	2.80e+03
	869.7	16619008	3	7.373e+05	3.09e+03
HD098230	869.7	16619264	3	1.467e+05	4.65e+02
HD098553	301.2	5408512	3	3.858e+03	3.39e+01
HD100167	463.9	5420544	3	5.036e+03	3.57e+01
HD101452	664.8	15247104	3	1.910e+03	3.50e+01
HD101472	518.8	5343232	3	3.834e+03	3.44e+01
HD101959	301.2	5419008	3	5.822e+03	3.20e+01
HD102647	302.5	9940736	3	2.372e+05	7.01e+02
	869.7	16618752	3	2.358e+05	7.39e+02
HD102870	298.4	9940992	3	1.309e+05	5.02e+02
HD105805	278.5	3991808	3	5.734e+03	5.10e+01
HD106252	284.1	5442816	3	4.749e+03	3.73e+01
HD106965	521.7	13201920	3	1.248e+03	1.87e+01
HD108799	322.4	5338624	3	1.242e+04	4.16e+01
HD108944	518.7	5334784	3	4.431e+03	3.10e+01
HD109612	524.6	13111808	3	1.260e+04	6.56e+01
HD109866	524.9	13112064	3	4.368e+03	2.77e+01
HD110304	905.9	16869376	3	1.510e+05	5.70e+02
HD112196	492.2	5278976	3	6.345e+03	3.41e+01
HD115043	281.5	6599168	3	7.863e+03	3.29e+01
HD115780	563.2	13380864	3	1.022e+04	1.25e+02
	563.3	13383680	3	1.064e+04	1.38e+02
HD116706	279.6	3994624	3	6.188e+03	5.01e+01
HD119545	551.8	13313024	3	1.360e+05	2.33e+03
HD121370	905.8	16836608	3	3.132e+05	1.17e+03
HD121504	340.5	5438208	3	4.016e+03	4.34e+01
HD122652	302.0	5428224	3	5.100e+03	2.87e+01
HD123123	905.9	16869632	3	6.343e+05	2.39e+03
HD127665	181.2	9059328	3	6.687e+05	2.51e+03
HD128998	671.5	15247360	3	4.824e+03	2.79e+01
HD129655	705.6	15421696	3	2.577e+03	2.87e+01
HD131986	551.8	13313280	3	7.721e+03	9.91e+01
HD132417	551.7	13313536	3	5.041e+03	5.49e+01
HD132439	551.7	13313792	3	5.055e+03	3.77e+01
HD134493	202.1	9191936	3	2.956e+04	1.24e+02
HD138265	96.9	7972352	3	1.447e+05	5.20e+02
	202.1	9191680	3	1.443e+05	7.25e+02
HD139698	551.7	13314048	3	8.006e+03	1.99e+02
HD141937	345.4	5442048	3	5.126e+03	3.82e+01
HD144873	671.6	15247616	3	1.723e+03	1.96e+01
HD150680	364.5	11892480	3	3.335e+05	1.33e+03
HD150706	110.2	5386240	3	6.656e+03	3.12e+01
HD152222	96.9	7971584	3	5.203e+04	3.13e+02
	1136.3	20459520	3	5.187e+04	4.66e+01
	1136.3	20459776	10	5.142e+04	2.11e+01
HD153458	387.1	5416704	3	2.799e+03	3.91e+01
HD154391	96.9	7970560	3	3.023e+04	1.22e+02
HD158460	96.9	7970048	3	7.931e+03	5.71e+01
HD158485	96.9	7969280	3	3.564e+03	2.80e+01
HD159048	96.9	7970816	3	3.600e+04	1.88e+02

TABLE 2 — *Continued*

Name	days since mission start	AORKEY[a]	DCE[b] time (s)	count rate (DN/s)	uncertainty (DN/s)
HD159222	320.9	5436672	3	9.997e+03	2.90e+01
	634.1	13590016	3	9.787e+03	5.20e+01
	1134.3	20462080	3	1.019e+04	4.86e+01
	1134.3	20462336	10	9.952e+03	2.10e+01
	1134.3	20462592	30	1.020e+04	1.36e+01
HD159330	42.5	6941696	3	7.978e+04	2.77e+02
	49.5	7143424	3	7.977e+04	3.18e+02
	49.5	7143680	3	7.957e+04	3.26e+02
	49.6	7143936	3	7.953e+04	3.27e+02
	49.6	7144192	3	7.934e+04	3.20e+02
	49.6	7144448	3	7.936e+04	3.06e+02
	53.8	7166976	3	8.024e+04	2.92e+02
	60.9	7200512	3	7.975e+04	2.96e+02
	61.4	7202048	3	8.030e+04	2.86e+02
	70.7	7337728	3	7.946e+04	2.95e+02
	69.4	7346688	3	7.951e+04	4.85e+02
	69.0	7348736	3	7.933e+04	2.79e+02
	73.4	7428608	3	7.980e+04	2.98e+02
	73.4	7430144	10	8.084e+04	3.96e+02
	58.8	7640320	3	7.979e+04	2.96e+02
	69.8	7744256	3	7.967e+04	2.97e+02
	90.6	7795712	3	7.915e+04	2.96e+02
	96.5	7974400	3	7.913e+04	2.87e+02
	84.1	7978752	3	7.963e+04	2.96e+02
	84.1	7980544	3	7.959e+04	2.94e+02
	104.8	8137216	3	7.927e+04	2.90e+02
	106.8	8137984	3	7.995e+04	3.03e+02
	107.9	8342016	3	7.977e+04	2.96e+02
	125.8	8379904	3	7.914e+04	2.91e+02
	127.2	8380672	3	7.958e+04	2.82e+02
	109.9	8782592	3	7.947e+04	2.84e+02
	153.5	8809472	3	7.964e+04	3.04e+02
	157.0	8819200	3	7.977e+04	2.99e+02
	162.1	8937472	3	7.979e+04	2.90e+02
	178.8	9066496	3	7.905e+04	2.90e+02
	182.2	9066752	3	7.926e+04	2.98e+02
	185.1	9181440	3	7.952e+04	3.00e+02
	201.7	9190912	3	7.900e+04	2.88e+02
	205.6	9221632	3	7.964e+04	3.01e+02
	209.5	9222400	3	7.960e+04	3.10e+02
	224.7	9457408	3	7.913e+04	3.00e+02
	231.9	9617664	3	7.928e+04	3.09e+02
	228.9	9640192	3	7.915e+04	3.16e+02
	250.7	9658368	3	7.918e+04	3.11e+02
	253.5	9658880	3	7.932e+04	3.02e+02
	258.0	9659392	3	7.937e+04	3.02e+02
	276.9	9802496	3	7.919e+04	3.11e+02
	281.7	9803264	3	7.919e+04	3.03e+02
	284.5	9804032	3	7.939e+04	3.17e+02
	298.2	9937152	3	7.898e+04	3.08e+02
	300.6	9938688	3	7.924e+04	3.19e+02
	303.5	9939456	3	7.910e+04	3.11e+02
	317.6	10087936	3	7.891e+04	2.99e+02
	319.7	10088704	3	7.931e+04	3.21e+02
	322.5	10089472	3	7.911e+04	3.08e+02
	338.6	11780352	3	7.878e+04	2.98e+02
	342.1	11781120	3	7.929e+04	3.11e+02
	345.1	11781888	3	7.969e+04	3.04e+02
	347.4	11782656	3	7.914e+04	2.95e+02
	359.7	11891200	3	7.911e+04	3.04e+02
	362.6	11897088	3	7.930e+04	3.11e+02
	368.0	11897856	3	7.930e+04	3.04e+02
	385.6	12060160	3	7.883e+04	2.99e+02
	389.5	12060928	3	7.921e+04	3.07e+02
	393.0	12061696	3	7.947e+04	2.98e+02
	397.8	12152832	3	7.941e+04	3.00e+02
	414.5	12194560	3	7.885e+04	2.85e+02
	418.0	12195328	3	7.875e+04	3.06e+02
	421.5	12196096	3	7.921e+04	2.99e+02
	438.8	12394496	3	7.934e+04	2.96e+02
	434.5	12395264	3	7.917e+04	2.96e+02
	443.4	12396032	3	7.952e+04	3.02e+02
	516.6	13108992	3	7.879e+04	2.88e+02
	529.4	13110016	3	7.901e+04	2.99e+02
	521.7	13111040	3	7.887e+04	3.04e+02

TABLE 2 — *Continued*

Name	days since mission start	AORKEY[a]	DCE[b] time (s)	count rate (DN/s)	uncertainty (DN/s)
	550.6	13295360	3	7.862e+04	2.90e+02
	557.8	13298176	3	7.933e+04	3.03e+02
	563.1	13299200	3	7.904e+04	3.02e+02
	584.5	13428992	3	7.880e+04	2.96e+02
	591.0	13431552	3	7.863e+04	2.97e+02
	596.6	13432320	3	7.905e+04	3.13e+02
	634.3	13585408	3	7.937e+04	3.14e+02
	624.6	13586176	3	7.866e+04	2.98e+02
	629.4	13586944	3	7.908e+04	3.02e+02
	634.4	13587712	3	7.944e+04	3.08e+02
	660.6	15217152	3	7.896e+04	3.01e+02
	667.8	15220480	3	7.917e+04	3.14e+02
	701.5	15413248	3	7.889e+04	3.00e+02
	704.9	15414272	3	7.898e+04	3.10e+02
	709.3	15415296	3	7.920e+04	3.09e+02
	731.6	15815168	3	7.899e+04	2.98e+02
	735.9	15816192	3	7.927e+04	3.04e+02
	742.1	15817216	3	7.919e+04	3.03e+02
	760.4	15991040	3	7.854e+04	3.04e+02
	767.9	16047616	3	7.916e+04	3.06e+02
	775.9	16048640	3	7.901e+04	2.95e+02
	800.4	16228608	3	7.868e+04	2.89e+02
	805.8	16254208	3	7.924e+04	3.00e+02
	810.8	16255232	3	7.925e+04	2.92e+02
	869.6	16603648	3	7.914e+04	2.92e+02
	872.1	16604416	3	7.909e+04	3.01e+02
	869.6	16619520	3	7.898e+04	2.96e+02
	904.0	16833792	3	7.899e+04	2.95e+02
	910.8	16834816	3	7.905e+04	2.91e+02
	921.2	16835840	3	7.883e+04	2.98e+02
	1134.3	20459008	3	7.921e+04	4.95e+01
	1134.3	20459264	10	7.932e+04	2.15e+01
HD163466	96.9	7969024	3	2.952e+03	2.48e+01
	465.5	12872448	3	2.963e+03	3.71e+01
	630.4	13613824	3	2.841e+03	4.81e+01
HD163588	97.0	7973376	3	4.503e+05	1.62e+03
	298.5	9942528	3	4.427e+05	2.42e+03
HD165459	96.9	7968256	3	3.830e+03	3.82e+01
	283.0	9851392	3	3.853e+03	3.26e+01
HD166780	96.9	7970304	3	3.072e+04	1.20e+02
	254.7	9660416	3	3.057e+04	1.30e+02
HD167389	303.3	5434368	3	4.449e+03	2.66e+01
HD170693	96.9	7971840	3	1.905e+05	6.87e+02
	905.8	16869888	3	1.877e+05	6.81e+02
	1136.3	20458496	3	1.830e+05	4.73e+01
	1136.3	20458752	10	1.861e+05	2.40e+01
HD172066	96.9	7968512	3	3.368e+03	2.68e+01
HD172728	96.9	7969792	3	4.754e+03	3.21e+01
	465.5	12872704	3	4.741e+03	3.04e+01
HD173398	461.6	12871424	3	3.019e+04	1.21e+02
	466.6	12884224	3	3.050e+04	1.22e+02
	470.4	12884736	3	3.048e+04	1.26e+02
	484.6	12997120	3	3.014e+04	1.20e+02
	488.8	13001472	3	3.041e+04	1.24e+02
	496.4	13071872	10	3.082e+04	1.52e+02
	496.4	13072128	30	3.120e+04	1.52e+02
	496.5	13072640	3	3.030e+04	1.16e+02
	516.6	13108736	3	3.014e+04	1.15e+02
	529.4	13109760	3	3.016e+04	1.21e+02
	521.8	13110784	3	3.033e+04	1.23e+02
	550.5	13295104	3	3.013e+04	1.18e+02
	557.8	13297920	3	3.028e+04	1.22e+02
	563.0	13298944	3	3.020e+04	1.25e+02
	584.5	13428736	3	3.018e+04	1.22e+02
	591.0	13431296	3	3.016e+04	1.26e+02
	596.6	13432064	3	3.048e+04	1.32e+02
	634.3	13585152	3	3.043e+04	1.27e+02
	624.6	13585920	3	3.018e+04	1.24e+02
	629.4	13586688	3	3.026e+04	1.23e+02
	634.4	13587456	3	3.035e+04	1.28e+02
	660.6	15216896	3	3.006e+04	1.24e+02
	667.8	15220224	3	3.036e+04	1.26e+02
	674.2	15221248	3	3.043e+04	1.29e+02
	701.5	15412992	3	3.022e+04	1.23e+02
	704.9	15414016	3	3.036e+04	1.25e+02

TABLE 2 — *Continued*

Name	days since mission start	AORKEY[a]	DCE[b] time (s)	count rate (DN/s)	uncertainty (DN/s)
	709.3	15415040	3	3.047e+04	1.29e+02
	731.6	15814912	3	3.030e+04	1.21e+02
	735.9	15815936	3	3.031e+04	1.26e+02
	742.1	15816960	3	3.040e+04	1.28e+02
	760.4	15990784	3	3.000e+04	1.21e+02
	767.9	16047360	3	3.034e+04	1.27e+02
	775.9	16048384	3	3.023e+04	1.25e+02
	800.4	16228352	3	3.009e+04	1.22e+02
	805.8	16253952	3	3.076e+04	1.28e+02
	810.8	16254976	3	3.035e+04	1.19e+02
	827.8	16374528	3	3.000e+04	1.17e+02
	830.8	16375296	3	3.030e+04	1.22e+02
	835.9	16376832	3	3.031e+04	1.21e+02
	864.7	16602624	3	3.008e+04	1.18e+02
	869.6	16603392	3	3.043e+04	1.19e+02
	872.0	16604160	3	3.045e+04	1.23e+02
	904.0	16833536	3	3.037e+04	1.20e+02
	910.8	16834560	3	3.030e+04	2.03e+02
	921.2	16835584	3	3.040e+04	1.25e+02
	905.8	16870144	3	3.025e+04	1.28e+02
HD173511	96.9	7971072	3	3.165e+04	1.24e+02
HD173976	96.9	7971328	3	4.749e+04	1.72e+02
HD174123	96.9	7968000	3	2.296e+03	2.39e+01
HD176841	96.9	7968768	3	3.644e+03	2.79e+01
HD180711	97.0	7973632	3	5.796e+05	2.09e+03
	280.7	9805568	3	5.722e+05	2.07e+03
HD183439	70.7	7334144	3	7.201e+05	3.67e+03
	70.8	7335424	3	7.198e+05	3.81e+03
HD189276	97.0	7973120	3	3.868e+05	1.38e+03
	280.7	9805824	3	3.844e+05	1.51e+03
HD191854	96.9	7969536	3	5.075e+03	4.82e+01
	254.7	9660672	3	4.652e+03	3.60e+01
	254.7	9661184	10	4.922e+03	2.69e+01
HD193017	415.0	5410560	3	4.150e+03	3.86e+01
HD195034	439.3	5426688	3	6.127e+03	3.33e+01
HD199598	301.8	5413632	3	7.021e+03	3.60e+01
HD201941	280.7	9806080	3	2.900e+03	2.79e+01
HD204277	435.3	5374976	3	7.301e+03	2.83e+01
HD205905	417.6	5405440	3	7.871e+03	3.42e+01
HD209952	69.4	7345152	3	1.468e+05	5.43e+02
	84.0	7979008	3	1.462e+05	5.16e+02
HD212291	441.9	5421312	3	3.319e+03	3.19e+01
HD216131	96.9	7972608	3	3.277e+05	1.24e+03
HD216275	318.5	5435136	3	5.062e+03	4.07e+01
HD217382	97.0	7972864	3	3.264e+05	1.18e+03
NPM1+61.0569	465.5	12872960	3	1.510e+03	1.64e+01
NPM1+68.0412	415.5	12196864	3	1.494e+03	1.67e+01
SAO9310	415.5	12197120	3	1.069e+03	1.24e+01

[a] The "AORKEY," or Astronomical Observation Request Key, is used by the *Spitzer* Science Center to uniquely identify the observation.
[b] "DCE" refers to "Data Collection Event," in this case an individual image.

TABLE 3
DATA USED TO COMPUTE THE 24 μM CALIBRATION FACTOR

Name	K_s[a] (mag.)	24μm count rate (DN/s)	uncertainty (DN/s)	calibration factor (MJy/sr/[DN/s])	uncertainty (MJy/sr/[DN/s])
HD000319	5.479	6.708e+03	5.00e+01	4.513e−02	1.39e−03
HD002811	7.057	1.591e+03	3.35e+01	4.448e−02	1.63e−03
HD011413	5.422	7.866e+03	3.87e+01	4.056e−02	1.23e−03
HD014943	5.439	7.180e+03	2.84e+01	4.374e−02	1.32e−03
HD015646	6.411	2.997e+03	4.85e+01	4.281e−02	1.46e−03
HD017254	5.877	4.529e+03	1.97e+01	4.632e−02	1.40e−03
HD020888	5.691	5.519e+03	2.04e+01	4.512e−02	1.36e−03
HD021981	5.526	6.089e+03	1.33e+01	4.761e−02	1.43e−03
HD034868	6.024	3.851e+03	3.89e+01	4.758e−02	1.51e−03
HD042525	5.751	5.116e+03	2.85e+01	4.606e−02	1.40e−03
HD057336	7.114	1.403e+03	3.44e+01	4.786e−02	1.86e−03
HD073210	6.165	3.707e+03	5.55e+01	4.341e−02	1.45e−03
HD073666	6.532	2.541e+03	5.66e+01	4.517e−02	1.69e−03
HD073819	6.280	3.170e+03	5.29e+01	4.566e−02	1.57e−03
HD092845	5.513	7.166e+03	4.51e+01	4.094e−02	1.26e−03
HD101452	6.819	1.910e+03	3.50e+01	4.613e−02	1.62e−03
HD105805	5.600	5.734e+03	5.10e+01	4.722e−02	1.48e−03
HD116706	5.502	6.188e+03	5.01e+01	4.789e−02	1.49e−03
HD128998	5.756	4.824e+03	2.79e+01	4.862e−02	1.48e−03
HD158485	6.145	3.564e+03	2.79e+01	4.599e−02	1.43e−03
HD163466	6.339	2.917e+03	2.94e+01	4.699e−02	1.49e−03
HD172728	5.753	4.747e+03	2.21e+01	4.954e−02	1.50e−03

NOTE. — The average calibration factor is 4.54×10^{-2} MJy sr^{-1} (DN/s)$^{-1}$, to which we've assigned an uncertainty of 2% (see § 3).

[a] K_s =[24] for the stars in this table (see Rieke et al. 2007), all of which are between types A0 and A6.

TABLE 4
Zero-point Conversions

Data Set	Conversion Factor
2MASS saturated J	-0.053 mag.
2MASS saturated K_s	-0.035 mag.
Johnson J	-0.025 mag.
Johnson K	-0.035 mag.
IRAS 12 μm	$\times 0.266$
IRAS 25 μm	$\times 1.11$

Note. — These factors convert measurements to 24 μm magnitudes (NIR) or fluxes (IRAS) (see § 4.1).

TABLE 5
MIPS Stellar Flux Calibrator Sample.

Name	Spectral Type	super-K_s[a] (mag.)	unc. (mag.)	$f_\nu(12\mu m)$[b] (Jy)	unc. (Jy)	$f_\nu(25\mu m)$[b] (Jy)	unc. (Jy)	predictions			
								$f_\nu(24\mu m)$[c] (Jy)	unc. (Jy)	bkgd$_{24}$[d] (MJy/sr)	unc. (MJy/sr)
BD+621644	K5	5.258	0.013					6.355e−02	1.50e−03	1.54e+01	2.38e+00
HD000319	A1V	5.541	0.014					4.356e−02	1.14e−03	3.43e+01	6.33e+00
HD001160	A0	7.020	0.018					1.116e−02	3.17e−04	4.92e+01	1.34e+01
HD001644	K0III	5.370	0.016	2.700e−01	3.24e−02			5.659e−02	1.52e−03	4.99e+01	1.37e+01
HD001753	F5V	7.730	0.017					6.047e−03	1.83e−04	1.81e+01	2.37e+00
HD002151	G2IV	1.307	0.193	8.471e+00	3.39e−01	2.099e+00	1.05e−01	2.279e+00	7.22e−02	1.72e+01	2.59e+00
HD002261	K0III	−0.143	0.223	3.866e+01	2.71e+00	9.149e+00	6.40e−01	1.010e+01	4.95e−01	2.27e+01	2.91e+00
HD002811	A3V	7.086	0.017					1.050e−02	2.92e−04	2.21e+01	2.73e+00
HD003712	K0IIIa	−0.308	0.028					1.048e+01	3.75e−01	1.97e+01	3.90e+00
HD004128	K0III	−0.323	0.028	4.320e+01	2.59e+00	9.303e+00	5.58e−01	1.070e+01	2.95e−01	3.45e+01	5.88e+00
HD006860	M0III	−1.897	0.028	2.000e+02	1.40e+01	4.618e+01	3.23e+00	4.711e+01	1.38e+00	2.75e+01	6.10e+00
HD008941	F8V	5.356	0.014	2.500e−01	3.00e−02			5.430e−02	1.52e−03	4.51e+01	1.22e+01
HD009053	M0IIIa	−0.480	0.204	5.187e+01	2.59e+00	1.178e+01	5.89e−01	1.329e+01	4.75e−01	2.03e+01	1.68e+00
HD009927	K3III	0.681	0.028	1.618e+01	8.09e−01	3.651e+00	1.83e−01	4.181e+00	1.07e−01	2.31e+01	5.07e+00
HD011413	A1V	5.484	0.013	1.993e−01	2.19e−02			4.622e−02	1.15e−03	1.85e+01	1.16e+00
HD012533	K3IIb	−0.824	0.028	6.979e+01	3.49e+00	1.672e+01	8.36e−01	1.756e+01	4.48e−01	2.69e+01	6.32e+00
HD012929	K2III	−0.715	0.028	5.904e+01	2.95e+00	1.401e+01	8.40e−01	1.537e+01	4.06e−01	4.24e+01	1.16e+01
HD014943	A5V	5.481	0.018	1.647e−01	1.32e−02			4.586e−02	1.23e−03	1.77e+01	8.12e−01
HD015008	A1/2V	3.995	0.124	7.404e−01	2.96e−02	1.696e−01	1.36e−02	1.971e−01	6.92e−03	1.62e+01	2.00e+00
HD015646	A0V	6.394	0.015					1.986e−02	5.29e−04	1.64e+01	1.76e+00
HD017254	A2V	5.923	0.013	1.275e−01	1.66e−02			3.076e−02	7.72e−04	1.73e+01	8.88e−01
HD017709	K5III	0.727	0.028	1.624e+01	8.12e−01	3.946e+00	2.37e−01	4.152e+00	1.10e−01	3.48e+01	9.17e+00
HD018884	M1.5III	−1.730	0.028	1.634e+02	6.54e+00	3.954e+01	1.98e+00	4.100e+01	9.82e−01	4.26e+01	9.55e+00
HD019019	F8	5.563	0.017	1.714e−01	2.06e−02			4.456e−02	1.31e−03	4.45e+01	1.04e+01
HD020644	K4III	0.807	0.158	1.494e+01	7.47e−01	3.502e+00	1.75e−01	3.895e+00	1.38e−01	4.39e+01	1.22e+01
HD020722	K3.5III	6.010	0.015	1.234e−01	1.48e−02			3.118e−02	8.17e−04	1.81e+01	1.01e+00
HD020888	A3V	5.722	0.017	1.471e−01	1.47e−02			3.706e−02	9.94e−04	1.59e+01	1.99e+00
HD020902	F5I	0.490	0.028					4.566e+00	1.63e−01	2.70e+01	6.37e+00
HD021981	A1V	5.590	0.019	1.421e−01	1.14e−02			4.126e−02	1.13e−03	1.69e+01	9.66e−01
HD022686	A0	7.154	0.015					9.861e−03	2.63e−04	3.86e+01	8.43e+00
HD024512	M2III	−1.003	0.244	8.013e+01	3.21e+00	1.972e+01	7.89e−01	2.136e+01	6.24e−01	1.59e+01	2.26e+00
HD025025	M1IIIb	−1.022	0.028	7.756e+01	3.88e+00	1.917e+01	9.59e−01	2.048e+01	5.22e−01	2.58e+01	4.15e+00
HD025860	A4/5IV	6.112	0.014	1.064e−01	1.70e−02			2.581e−02	6.65e−04	1.64e+01	1.39e+00
HD027466	G5	6.274	0.014	1.170e−01	2.11e−02			2.323e−02	6.59e−04	3.03e+01	6.02e+00
HD028099	G2V	6.547	0.016					1.798e−02	5.35e−04	5.00e+01	1.30e+01
HD028471	G5V	6.323	0.017	9.760e−02	1.56e−02			2.219e−02	6.61e−04	1.54e+01	1.90e+00
HD029139	K5III	−2.868	0.028	4.468e+02	2.23e+01	1.059e+02	6.36e+00	1.135e+02	3.00e+00	4.98e+01	1.29e+01
HD029461	G5V	6.436	0.021					1.991e−02	6.51e−04	4.79e+01	1.22e+01
HD030246	G5V	6.725	0.021					1.526e−02	4.99e−04	4.83e+01	1.26e+01
HD031398	K3II	−0.607	0.028					1.380e+01	4.94e−01	4.52e+01	1.25e+01
HD032384	G5V	7.121	0.015					1.060e−02	3.10e−04	1.53e+01	2.06e+00
HD032831	K3III	1.721	0.028	5.984e+00	1.79e−01	1.408e+00	4.22e−02	1.581e+00	3.03e−02	1.79e+01	2.44e+00
HD032887	K4III	−0.285	0.028	3.936e+01	1.97e+00	9.121e+00	5.47e−01	1.025e+01	2.71e−01	2.10e+01	3.42e+00
HD034029	G5IIIe+	−1.898	0.028					4.532e+01	1.62e+00	3.29e+01	8.25e+00
HD034377	G5V	7.183	0.036	6.193e−02	1.05e−02			1.016e−02	4.34e−04	1.55e+01	1.97e+00
HD034868	A0V	6.014	0.019	9.262e−02	1.94e−02			2.811e−02	8.10e−04	1.95e+01	3.05e+00
HD035666	K3III	3.829	0.135	9.167e−01	3.67e−02	2.113e−01	1.27e−02	2.383e−01	7.88e−03	1.58e+01	2.32e+00
HD036167	K5III	0.772	0.205			3.309e+00	1.99e−01	3.688e+00	2.18e−01	3.19e+01	7.04e+00
HD037962	G4V	6.288	0.015	8.465e−02	2.03e−02			2.282e−02	6.62e−04	1.85e+01	3.01e+00
HD038921	A0V	7.521	0.014					7.033e−03	1.84e−04	1.74e+01	2.64e+00
HD038944	M0III	0.634	0.028					4.401e+00	1.58e−01	4.16e+01	1.12e+01
HD038949	G1V	6.424	0.018					2.013e−02	6.22e−04	2.00e+01	3.57e+00
HD039425	K2III	0.444	0.028	2.030e+01	1.01e+00	4.530e+00	2.27e−01	5.210e+00	1.33e−01	1.78e+01	2.73e+00
HD039608	K5III	3.803	0.120	1.014e+00	4.06e−02	2.358e−01	1.41e−02	2.621e−01	8.61e−03	1.55e+01	2.14e+00
HD040129	G5V	6.807	0.016	6.654e−02	1.13e−02			1.422e−02	4.17e−04	1.57e+01	1.77e+00
HD040335	A1II	6.434	0.015					1.914e−02	5.10e−04	3.45e+01	8.00e+00
HD041371	K0III	4.742	0.019	3.750e−01	1.50e−02	9.177e−02	7.34e−03	9.982e−02	2.28e−03	1.55e+01	2.22e+00
HD042525	A0V	5.768	0.016	1.186e−01	7.12e−03			3.477e−02	8.64e−04	1.55e+01	2.26e+00
HD042701	K3III	3.595	0.217	1.134e+00	2.27e−02	2.724e−01	8.17e−03	2.990e−01	5.41e−03	1.55e+01	2.28e+00
HD043107	B8V	5.197	0.013	2.085e−01	1.04e−02			5.942e−02	1.36e−03	1.55e+01	2.31e+00
HD044431	G5V	4.330	0.131	8.992e−01	2.70e−02	2.372e−01	9.49e−03	2.355e−01	5.87e−03	1.66e+01	2.73e+00
HD044594	G3V	5.119	0.019	2.399e−01	1.44e−02	6.873e−02	1.24e−02	6.641e−02	1.83e−03	1.63e+01	2.40e+00
HD045348	F0II	−1.403	0.028	1.064e+02	3.19e+00	2.524e+01	7.57e−01	2.763e+01	5.29e−01	1.62e+01	2.19e+00
HD045557	A0V	5.763	0.012	1.230e−01	1.23e−02			3.538e−02	8.61e−04	1.56e+01	2.31e+00
HD046190	A0V	6.396	0.015	7.604e−02	1.14e−02			1.985e−02	5.21e−04	1.56e+01	2.33e+00
HD046819	K0III	5.302	0.015	2.249e−01	1.35e−02	7.168e−02	1.08e−02	5.996e−02	1.45e−03	1.55e+01	2.36e+00
HD047332	A1IV	6.687	0.013	8.042e−02	1.45e−02			1.523e−02	3.86e−04	1.59e+01	2.61e+00
HD048002	A5IV	7.406	0.015					7.818e−03	2.08e−04	1.65e+01	2.38e+00
HD048915	A0V	−1.400	0.120					2.603e+01	3.18e+00	2.33e+01	4.84e+00
HD050310	K1III	0.335	0.200	2.312e+01	9.25e−01	5.862e+00	2.35e−01	6.265e+00	1.83e−01	1.66e+01	2.29e+00
HD051799	M1III	0.511	0.028	2.069e+01	8.28e−01	5.032e+00	2.01e−01	5.236e+00	1.19e−01	1.66e+01	2.40e+00
HD053501	K3III	2.084	0.202	4.718e+00	1.42e−01	1.180e+00	3.54e−02	1.269e+00	2.86e−02	1.57e+01	2.48e+00
HD053811	A4IV	4.665	0.127	3.976e−01	1.59e−02	9.668e−02	1.16e−02	1.067e−01	3.96e−03	1.66e+01	2.46e+00

TABLE 5 — *Continued*

								predictions			
Name	Spectral Type	super-K_s[a] (mag.)	unc. (mag.)	$f_\nu(12\mu\mathrm{m})$[b] (Jy)	unc. (Jy)	$f_\nu(25\mu\mathrm{m})$[b] (Jy)	unc. (Jy)	$f_\nu(24\mu\mathrm{m})$[c] (Jy)	unc. (Jy)	bkgd_{24}[d] (MJy/sr)	unc. (MJy/sr)
HD056413	G5V	7.307	0.016					8.927e−03	2.66e−04	1.57e+01	2.65e+00
HD056855	K3Ib	−1.005	0.028	9.475e+01	3.79e+00	2.341e+01	9.37e−01	2.251e+01	5.16e−01	1.80e+01	3.34e+00
HD057336	A0IV	7.194	0.020					9.504e−03	2.83e−04	1.65e+01	2.72e+00
HD057507	G5V	7.114	0.018					1.066e−02	3.29e−04	1.56e+01	2.68e+00
HD058142	A1V	4.608	0.117	3.832e−01	2.30e−02			1.041e−01	5.62e−03	2.95e+01	6.98e+00
HD059717	K5III	−0.468	0.028	4.924e+01	2.46e+00	1.199e+01	5.99e−01	1.258e+01	3.21e−01	1.74e+01	2.83e+00
HD060178	A2V	1.431	0.028	7.211e+00	4.33e−01	1.624e+00	8.12e−02	1.893e+00	5.01e−02	4.50e+01	1.22e+01
HD060522	M0III	0.202	0.028	2.549e+01	1.27e+00	5.944e+00	2.38e−01	6.593e+00	1.59e−01	4.91e+01	1.33e+01
HD061929	G5V	6.366	0.014	7.234e−02	1.09e−02			2.115e−02	5.97e−04	1.55e+01	2.56e+00
HD062509	K0IIIb	−1.185	0.028	8.784e+01	3.51e+00	2.024e+01	1.01e+00	2.315e+01	5.54e−01	4.81e+01	1.30e+01
HD064324	G0	6.242	0.013					2.381e−02	6.73e−04	4.16e+01	1.10e+01
HD065517	A2/3IV	6.879	0.019					1.270e−02	3.70e−04	1.66e+01	2.79e+00
HD066751	F8	5.071	0.015	2.435e−01	1.95e−02			6.932e−02	1.91e−03	2.00e+01	3.84e+00
HD069863	A2V	4.954	0.014	3.275e−01	1.31e−02	7.684e−02	8.45e−03	7.822e−02	1.69e−03	1.55e+01	2.46e+00
HD070272	K4.5III	0.567	0.028	1.923e+01	9.62e−01	4.546e+00	2.27e−01	4.846e+00	1.24e−01	3.25e+01	7.63e+00
HD071129	K3III+	−1.696	0.119	1.723e+02	5.17e+00	4.329e+01	1.73e+00	4.563e+01	1.12e+00	1.58e+01	2.57e+00
HD073210	A5V	6.185	0.015					2.407e−02	6.42e−04	4.96e+01	1.31e+01
HD073666	A1V	6.516	0.015					1.775e−02	4.73e−04	4.95e+01	1.28e+01
HD073819	A6V	6.283	0.014					2.199e−02	5.74e−04	4.95e+01	1.29e+01
HD075223	A1V	7.279	0.026					8.789e−03	3.00e−04	2.00e+01	3.53e+00
HD077281	A2	7.021	0.016					1.115e−02	3.03e−04	3.44e+01	9.28e+00
HD080007	A2IV	1.440	0.199	6.683e+00	2.67e−01	1.589e+00	6.36e−02	1.793e+00	5.22e−02	1.56e+01	2.61e+00
HD080493	K7III	−0.667	0.028	5.859e+01	2.93e+00	1.376e+01	8.26e−01	1.490e+01	3.94e−01	3.74e+01	8.71e+00
HD081797	K3II-III	−1.236	0.028	1.077e+02	6.46e+00	2.368e+01	1.42e+00	2.556e+01	7.06e−01	3.03e+01	7.64e+00
HD082308	K5III	0.567	0.028	2.031e+01	1.83e+00	4.486e+00	2.69e−01	4.798e+00	1.41e−01	4.76e+01	1.21e+01
HD082621	A2V	4.454	0.102	5.327e−01	3.20e−02			1.361e−01	7.16e−03	2.49e+01	4.74e+00
HD082668	K5III	−0.507	0.140					1.259e+01	1.78e+00	1.85e+01	2.60e+00
HD087901	B7	1.508	0.028	6.272e+00	3.14e−01	1.466e+00	1.47e−01	1.765e+00	4.94e−02	4.97e+01	1.36e+01
HD089388	K3IIa	0.091	0.227					7.256e+00	1.66e+00	1.71e+01	2.68e+00
HD089484	K1IIIb	−0.705	0.028	6.156e+01	2.46e+00	1.378e+01	5.51e−01	1.547e+01	3.52e−01	4.68e+01	1.14e+01
HD089758	M0III	−0.967	0.028	7.416e+01	3.71e+00	1.775e+01	1.06e+00	1.936e+01	5.11e−01	2.85e+01	5.26e+00
HD091056	M0III	0.748	0.216					3.962e+00	8.60e−01	1.69e+01	2.77e+00
HD091375	A1V	4.696	0.320	4.151e−01	2.08e−02	1.081e−01	1.40e−02	1.134e−01	5.31e−03	1.62e+01	2.86e+00
HD092305	M0III	0.330	0.193	2.491e+01	9.97e−01	6.116e+00	3.06e−01	6.592e+00	2.09e−01	1.69e+01	2.95e+00
HD092788	G5	5.733	0.023					3.805e−02	1.29e−03	4.22e+01	1.17e+01
HD092845	A0V	5.548	0.015	1.815e−01	3.08e−02			4.340e−02	1.14e−03	2.17e+01	4.09e+00
HD093813	K0/K1III	0.285	0.028	2.491e+01	1.49e+00	5.712e+00	4.00e−01	6.207e+00	1.76e−01	3.02e+01	6.93e+00
HD095418	A1V	2.248	0.028	3.320e+00	1.33e−01	9.755e−01	4.88e−02	9.326e−01	2.23e−02	2.12e+01	3.07e+00
HD095578	M0III	0.769	0.028	1.573e+01	1.10e+00	3.776e+00	2.27e−01	3.979e+00	1.13e−01	4.38e+01	1.22e+01
HD095689	K0Iab	−0.663	0.028	5.893e+01	2.36e+00	1.389e+01	6.94e−01	1.502e+01	3.59e−01	1.99e+01	2.80e+00
HD096833	K1III	0.389	0.028	2.111e+01	1.06e+00	5.086e+00	2.54e−01	5.556e+00	1.42e−01	2.49e+01	3.80e+00
HD098230	F8.5V	2.095	0.187	4.067e+00	2.03e−01	8.777e−01	5.27e−02	1.036e+00	3.98e−02	3.15e+01	5.38e+00
HD098262	K3III	0.269	0.028	2.457e+01	1.23e+00	5.808e+00	2.90e−01	6.296e+00	1.60e−01	3.05e+01	5.07e+00
HD098553	G2.5V	6.080	0.015	1.239e−01	1.61e−02			2.782e−02	7.94e−04	2.99e+01	6.51e+00
HD100029	M0III	−0.207	0.028	3.827e+01	1.53e+00	9.702e+00	4.85e−01	9.927e+00	2.38e−01	1.81e+01	2.53e+00
HD100167	F8	5.822	0.016	1.424e−01	1.71e−02			3.520e−02	1.02e−03	2.53e+01	3.60e+00
HD101452	A2	6.897	0.018					1.249e−02	3.55e−04	2.17e+01	3.49e+00
HD101472	G0	6.130	0.017	1.148e−01	1.95e−02			2.649e−02	7.91e−04	4.17e+01	1.10e+01
HD101959	G0V	5.617	0.015	1.486e−01	1.93e−02			4.218e−02	1.20e−03	2.55e+01	4.66e+00
HD102647	A3V	1.894	0.028	4.852e+00	2.91e−01			1.268e+00	3.90e−02	4.30e+01	9.18e+00
HD102870	F9V	2.226	0.179	3.622e+00	2.54e−01			9.641e−01	6.34e−02	5.00e+01	1.38e+01
HD105707	K2III	0.071	0.028	3.017e+01	1.81e+00	7.014e+00	4.21e−01	7.568e+00	2.09e−01	3.15e+01	6.42e+00
HD105805	A4V	5.607	0.022					4.099e−02	1.28e−03	3.05e+01	4.32e+00
HD106252	G0V	5.947	0.018	1.240e−01	1.86e−02			3.130e−02	9.47e−04	4.43e+01	9.84e+00
HD106965	A2	7.300	0.017					8.620e−03	2.40e−04	4.96e+01	1.31e+01
HD108799	G1.5V	4.864	0.016	3.295e−01	2.97e−02			8.498e−02	2.40e−03	4.19e+01	1.05e+01
HD108903	M3.5III	−3.196	0.098					1.498e+02	1.51e+01	2.05e+01	3.56e+00
HD108944	F8	5.997	0.012	1.408e−01	2.11e−02			3.000e−02	8.21e−04	2.68e+01	3.13e+00
HD109612	K1/K2III	5.067	0.014					7.419e−02	1.95e−03	2.50e+01	3.53e+00
HD109866	K0III	5.264	0.016					6.188e−02	1.70e−03	2.79e+01	3.55e+00
HD110304	A1IV	2.052	0.028	3.962e+00	1.98e−01	9.505e−01	4.75e−02	1.075e+00	2.73e−02	2.12e+01	3.93e+00
HD112196	F8V	5.553	0.017	1.769e−01	1.95e−02			4.505e−02	1.32e−03	3.02e+01	3.86e+00
HD115043	G1V	5.334	0.014	1.706e−01	1.71e−02			5.392e−02	1.49e−03	1.81e+01	1.51e+00
HD115780	G8/K0III	6.237	0.016					2.525e−02	6.93e−04	3.54e+01	3.83e+00
HD116706	A3IV	5.489	0.015	1.670e−01	2.50e−02			4.569e−02	1.20e−03	2.69e+01	2.89e+00
HD119545	K1III	6.077	0.013					2.926e−02	7.55e−04	6.54e+01	4.01e+00
HD120477	K5.5III	0.317	0.028	2.360e+01	1.42e+00	5.362e+00	3.22e−01	5.961e+00	1.64e−01	3.03e+01	4.43e+00
HD120933	K5III	0.150	0.028	3.300e+01	1.98e+00	7.983e+00	5.59e−01	7.377e+00	2.10e−01	2.15e+01	1.40e+00
HD121370	G0IV	1.272	0.028	9.781e+00	1.56e+00			2.328e+00	8.52e−02	2.83e+01	3.81e+00
HD121504	G2V	6.167	0.047					2.551e−02	1.36e−03	2.22e+01	4.45e+00
HD122652	F8	5.855	0.015	1.293e−01	1.94e−02			3.402e−02	9.76e−04	2.20e+01	1.74e+00
HD123123	K2III	0.634	0.028	1.644e+01	8.22e−01	3.837e+00	2.30e−01	4.352e+00	1.15e−01	3.90e+01	9.60e+00
HD123139	K0IIIb	−0.285	0.149	4.074e+01	2.04e+00	9.471e+00	5.68e−01	1.062e+01	4.03e−01	3.09e+01	7.05e+00
HD124897	K1.5III	−2.951	0.116	5.324e+02	4.79e+01	1.117e+02	7.82e+00	1.273e+02	6.46e+00	2.68e+01	3.57e+00

TABLE 5 — *Continued*

Name	Spectral Type	super-K_s[a] (mag.)	unc. (mag.)	$f_\nu(12\mu\mathrm{m})$[b] (Jy)	unc. (Jy)	$f_\nu(25\mu\mathrm{m})$[b] (Jy)	unc. (Jy)	predictions $f_\nu(24\mu\mathrm{m})$[c] (Jy)	unc. (Jy)	bkgd_{24}[d] (MJy/sr)	unc. (MJy/sr)
HD127665	K3III	0.582	0.028	1.773e+01	1.06e+00	4.187e+00	2.51e−01	4.631e+00	1.28e−01	2.15e+01	1.96e+00
HD128620	G2V	−1.922	0.146					4.389e+01	6.50e+00	3.59e+01	4.50e+00
HD128998	A1V	5.757	0.013	1.139e−01	1.14e−02			3.534e−02	8.76e−04	1.70e+01	7.99e−01
HD129078	K2.5III	0.679	0.210	1.737e+01	5.21e−01	4.261e+00	1.28e−01	4.636e+00	1.05e−01	1.78e+01	3.49e+00
HD129655	A2	6.702	0.018					1.495e−02	4.25e−04	4.17e+01	9.95e+00
HD131873	K4III	−1.359	0.141	1.137e+02	4.55e+00	2.693e+01	1.08e+00	2.974e+01	8.58e−01	1.56e+01	2.10e+00
HD131986	K0/K1III	6.852	0.016					1.433e−02	3.93e−04	4.98e+01	4.79e+00
HD132417	K0/K1III	6.388	0.013					2.197e−02	5.67e−04	4.74e+01	4.82e+00
HD132439	K2III	5.679	0.014					4.222e−02	1.11e−03	3.32e+01	4.88e+00
HD134493	K0III	3.922	0.120	8.047e−01	3.22e−02	1.775e−01	1.24e−02	2.083e−01	7.10e−03	1.68e+01	9.05e−01
HD136422	K5III	−0.171	0.231	3.514e+01	1.41e+00	8.305e+00	4.15e−01	9.214e+00	2.93e−01	3.61e+01	9.21e+00
HD137759	K2III	0.584	0.028	1.634e+01	6.54e−01	4.026e+00	1.61e−01	4.464e+00	1.02e−01	1.61e+01	1.25e+00
HD138265	K5III	1.523	0.177	3.644e+00	1.09e−01	9.313e−01	3.72e−02	9.848e−01	2.46e−02	1.60e+01	1.39e+00
HD139063	K5III	0.227	0.230	2.145e+01	1.07e+00	5.265e+00	3.16e−01	5.723e+00	2.21e−01	4.52e+01	1.24e+01
HD139698	G8/K0III	7.136	0.019					1.103e−02	3.23e−04	4.62e+01	5.78e+00
HD140573	K2IIIb	−0.036	0.028	2.850e+01	1.14e+00	7.028e+00	4.22e−01	7.836e+00	1.94e−01	2.99e+01	6.06e+00
HD141477	M0.5III	−0.016	0.028	3.110e+01	1.55e+00	7.606e+00	3.80e−01	8.139e+00	2.07e−01	2.36e+01	3.83e+00
HD141937	G2.5V	5.772	0.013	1.221e−01	1.71e−02			3.649e−02	1.01e−03	5.05e+01	1.40e+01
HD144873	G5	6.913	0.013					1.283e−02	3.63e−04	1.86e+01	2.16e+00
HD145829	K2III	5.142	0.018					6.923e−02	1.98e−03	6.27e+01	6.67e+00
HD146051	M0.5III	−1.281	0.028	1.077e+02	5.38e+00	2.600e+01	1.30e+00	2.693e+01	6.87e−01	3.69e+01	8.99e+00
HD149447	K6III	0.356	0.226					5.685e+00	1.29e+00	4.21e+01	1.13e+01
HD150039	K0III	4.872	0.013					8.878e−02	2.29e−03	6.09e+01	8.06e+00
HD150680	G0IV	1.174	0.183	9.061e+00	4.53e−01	2.246e+00	1.35e−01	2.447e+00	9.38e−02	1.87e+01	2.68e+00
HD150706	G0	5.559	0.018	1.571e−01	9.42e−03			4.401e−02	1.21e−03	1.58e+01	2.30e+00
HD150798	K2II-III	−1.140	0.133	1.036e+02	3.11e+00	2.355e+01	7.06e−01	2.655e+01	5.95e−01	2.04e+01	4.43e+00
HD151249	K5III	−0.039	0.242					8.179e+00	1.99e+00	2.40e+01	5.54e+00
HD151680	K2.5III	−0.389	0.140					1.129e+01	1.60e+00	4.35e+01	1.19e+01
HD152222	K2III	3.748	0.150	1.365e+00	8.19e−02	3.077e−01	1.85e−02	3.362e−01	1.40e−02	1.53e+01	2.00e+00
HD153210	K2III	0.549	0.028	1.735e+01	8.68e−01	4.033e+00	2.02e−01	4.635e+00	1.18e−01	2.60e+01	5.51e+00
HD153458	G0	6.456	0.013					1.955e−02	5.52e−04	3.98e+01	1.02e+01
HD154391	K2III	4.032	0.111	7.627e−01	2.29e−02	1.923e−01	9.61e−03	2.030e−01	5.28e−03	1.50e+01	2.02e+00
HD156283	K3Iab	−0.012	0.028	3.320e+01	1.33e+00	7.700e+00	3.85e−01	8.321e+00	1.99e−01	1.74e+01	2.71e+00
HD158460	A2V	5.489	0.013	1.610e−01	8.05e−03			4.529e−02	1.03e−03	1.53e+01	2.04e+00
HD158485	A4V	6.136	0.016	7.908e−02	8.70e−03			2.489e−02	6.59e−04	1.50e+01	1.76e+00
HD159048	K0III	4.122	0.236	8.951e−01	2.68e−02	2.302e−01	1.15e−02	2.391e−01	6.36e−03	1.56e+01	1.98e+00
HD159222	G5V	4.977	0.013	2.604e−01	1.56e−02			7.483e−02	1.92e−03	1.77e+01	2.99e+00
HD159330	K2III	2.867	0.146	2.065e+00	6.19e−02	4.976e−01	1.99e−02	5.467e−01	1.35e−02	1.49e+01	1.71e+00
HD161096	K2III	0.129	0.028	2.645e+01	1.32e+00	6.129e+00	3.06e−01	6.943e+00	1.77e−01	2.81e+01	6.63e+00
HD161743	B9IV	7.585	0.018					6.630e−03	1.89e−04	4.07e+01	1.10e+01
HD163376	M0III	0.748	0.229					3.962e+00	9.12e−01	3.65e+01	9.80e+00
HD163466	A2V	6.364	0.013	8.919e−02	1.07e−02			2.053e−02	5.14e−04	1.53e+01	2.16e+00
HD163588	K2III	0.971	0.028	1.165e+01	3.49e−01	2.853e+00	8.56e−02	3.142e+00	6.02e−02	1.49e+01	1.82e+00
HD164058	K5III	−1.408	0.028	1.106e+02	3.32e+00	2.713e+01	8.14e−01	2.931e+01	5.62e−01	1.56e+01	2.38e+00
HD165459	A2?	6.604	0.027	7.533e−02	1.20e−02			1.649e−02	5.62e−04	1.54e+01	2.21e+00
HD166780	K4.5III	3.792	0.101	7.866e−01	3.15e−02	1.919e−01	1.34e−02	2.104e−01	7.07e−03	1.49e+01	1.88e+00
HD167389	F8	5.908	0.015	1.118e−01	1.01e−02			3.210e−02	8.93e−04	1.66e+01	2.94e+00
HD169916	K1IIIb	0.298	0.028					5.997e+00	2.15e−01	5.08e+01	1.36e+01
HD170693	K1.5III	2.147	0.159	5.002e+00	1.50e−01	1.187e+00	3.56e−02	1.311e+00	2.95e−02	1.53e+01	2.31e+00
HD172066	G5?	6.279	0.015	8.687e−02	8.69e−03			2.302e−02	6.46e−04	1.54e+01	2.35e+00
HD172728	A0V	5.748	0.013	1.326e−01	1.06e−02			3.602e−02	8.78e−04	1.53e+01	2.36e+00
HD173398	K0III	4.003	0.213	8.061e−01	3.22e−02	1.912e−01	1.15e−02	2.120e−01	7.13e−03	1.54e+01	2.38e+00
HD173511	K5III	3.892	0.134	8.253e−01	2.48e−02	1.945e−01	9.73e−03	2.163e−01	5.67e−03	1.54e+01	2.39e+00
HD173976	K5III	3.572	0.177	1.186e+00	3.56e−02	2.966e−01	1.19e−02	3.163e−01	7.87e−03	1.53e+01	2.43e+00
HD174123	G5?	6.587	0.014	5.984e−02	8.98e−03			1.727e−02	4.87e−04	1.54e+01	2.39e+00
HD175510	A0V	4.960	0.124	2.920e−01	2.04e−02			7.833e−02	4.82e−03	2.76e+01	6.66e+00
HD176841	G5?	6.121	0.016	9.380e−02	1.22e−02			2.652e−02	7.69e−04	1.54e+01	2.44e+00
HD177716	K1IIIb	0.495	0.213	1.861e+01	9.30e−01	4.201e+00	2.10e−01	4.785e+00	1.71e−01	4.97e+01	1.38e+01
HD180093	K0Iab	5.081	0.015	5.662e+01	2.83e+00	1.862e+01	9.31e−01	7.340e−02	1.97e−03	4.44e+01	1.25e+01
HD180711	G9III	0.734	0.028	1.495e+01	4.49e−01	3.583e+00	1.08e−01	3.974e+00	7.62e−02	1.52e+01	2.74e+00
HD181655	G8V	4.625	0.013	3.838e−01	2.30e−02	9.729e−02	1.46e−02	1.097e−01	2.57e−03	1.73e+01	3.43e+00
HD183439	M0III	0.478	0.028					5.081e+00	1.82e−01	2.15e+01	4.37e+00
HD186791	K3II	−0.572	0.028					1.336e+01	4.78e−01	2.60e+01	6.18e+00
HD189276	K5Iab	0.785	0.168	9.434e+00	3.77e−01	2.417e+00	9.67e−02	2.581e+00	7.50e−02	1.54e+01	2.64e+00
HD191854	G5	5.808	0.015					3.551e−02	1.04e−03	1.92e+01	3.13e+00
HD193017	F8	5.949	0.013	1.381e−01	1.93e−02			3.134e−02	8.69e−04	3.73e+01	1.05e+01
HD195034	G5	5.547	0.017					4.516e−02	1.37e−03	2.14e+01	4.83e+00
HD197989	K0III	0.047	0.028					7.556e+00	2.70e−01	1.89e+01	3.86e+00
HD198542	M0III	0.209	0.198	2.784e+01	1.39e+00	6.685e+00	3.34e−01	7.318e+00	2.61e−01	4.70e+01	1.30e+01
HD199598	G0V	5.449	0.015	1.923e−01	1.54e−02			4.961e−02	1.36e−03	2.08e+01	4.47e+00
HD200914	K5/M0III	0.513	0.185	2.049e+01	1.23e+00	5.094e+00	3.06e−01	5.466e+00	2.30e−01	4.78e+01	1.32e+01
HD201941	A2	6.634	0.016					1.592e−02	4.33e−04	3.36e+01	8.94e+00
HD204277	F8V	5.416	0.015	2.114e−01	2.32e−02			5.124e−02	1.45e−03	2.54e+01	5.90e+00
HD205772	A5IV	7.651	0.013					6.239e−03	1.60e−04	3.13e+01	7.06e+00

TABLE 5 — *Continued*

Name	Spectral Type	super-K_s[a] (mag.)	unc. (mag.)	$f_\nu(12\mu\mathrm{m})$[b] (Jy)	unc. (Jy)	$f_\nu(25\mu\mathrm{m})$[b] (Jy)	unc. (Jy)	predictions $f_\nu(24\mu\mathrm{m})$[c] (Jy)	unc. (Jy)	bkgd_{24}[d] (MJy/sr)	unc. (MJy/sr)
HD205905	G4V	5.325	0.018	2.481e−01	2.98e−02			5.587e−02	1.67e−03	4.36e+01	1.15e+01
HD209750	G2Ib	0.917	0.028	1.383e+01	8.30e−01	3.014e+00	1.81e−01	3.430e+00	9.46e−02	4.08e+01	1.12e+01
HD209952	B7IV	2.003	0.213	3.743e+00	1.50e−01	8.486e−01	5.09e−02	1.014e+00	3.42e−02	2.64e+01	5.30e+00
HD211416	K3III	−0.330	0.183	4.280e+01	1.71e+00	1.024e+01	4.10e−01	1.128e+01	3.28e−01	2.12e+01	3.80e+00
HD212291	G5	6.263	0.020					2.335e−02	7.49e−04	3.29e+01	8.06e+00
HD213310	M0II+	0.158	0.028					6.822e+00	2.44e−01	1.76e+01	2.76e+00
HD216032	K5III	0.167	0.028	2.674e+01	1.60e+00	6.646e+00	3.99e−01	6.923e+00	1.91e−01	4.98e+01	1.35e+01
HD216131	G8II	1.374	0.028	8.362e+00	5.02e−01	1.989e+00	1.19e−01	2.217e+00	6.11e−02	2.51e+01	4.94e+00
HD216275	G0	5.782	0.013					3.637e−02	1.03e−03	1.77e+01	2.94e+00
HD217014	G2.5I	3.873	0.028	7.502e−01	4.50e−02	1.715e−01	2.23e−02	2.137e−01	6.42e−03	2.74e+01	5.67e+00
HD217382	K4III	1.471	0.193	8.334e+00	2.50e−01	1.936e+00	1.36e−01	2.176e+00	6.15e−02	1.75e+01	2.66e+00
HD217906	M2.5II	−2.190	0.028	2.702e+02	1.35e+01	6.888e+01	3.44e+00	6.472e+01	1.66e+00	2.41e+01	4.45e+00
HD60178J	A2V	1.431	0.028	7.211e+00	4.33e−01	1.624e+00	8.12e−02	1.893e+00	5.01e−02	4.50e+01	1.22e+01
HD98230J	G0V	2.090	0.187	4.069e+00	2.03e−01	8.779e−01	5.27e−02	1.036e+00	3.98e−02	3.15e+01	5.37e+00
NPM1+61.0569	K0.5III	7.210	0.013					1.031e−02	2.66e−04	1.53e+01	2.04e+00
NPM1+68.0412	K2III	7.169	0.015					1.070e−02	2.87e−04	1.54e+01	2.34e+00
SAO9310	K0	7.332	0.014					9.211e−03	2.42e−04	1.58e+01	2.41e+00

[a] Super-K_s is the weighted average of J (transformed to K_s) and K_s (see § 4.1).
[b] Taken from the IRAS Faint Source Catalog, and modified as discussed in § 4.1.3.
[c] These flux densities apply to the effective wavelength of the 24 μm band, 23.675 μm.
[d] See § 4.3.

TABLE 6
Combined Measurements and Calibration Factors

Name	number of measurements	24μm count rate[a] (DN/s)	uncertainty (DN/s)	calibration factor (MJy/sr/[DN/s])	uncertainty (MJy/sr/[DN/s])
BD+621644	1	1.033e+04	5.19e+01	4.037e−02	9.72e−04
HD000319	1	6.708e+03	5.00e+01	4.262e−02	1.16e−03
HD001160	1	1.395e+03	1.56e+01	5.250e−02	1.60e−03
HD001644	1	8.191e+03	5.69e+01	4.534e−02	1.25e−03
HD002151	1	3.271e+05	1.23e+03	4.573e−02	1.46e−03
HD002811	1	1.591e+03	3.35e+01	4.331e−02	1.51e−03
HD008941	1	7.202e+03	3.46e+01	4.948e−02	1.40e−03
HD009927	1	6.045e+05	2.45e+03	4.539e−02	1.17e−03
HD011413	1	7.866e+03	3.87e+01	3.856e−02	9.81e−04
HD014943	1	7.180e+03	2.84e+01	4.192e−02	1.14e−03
HD015008	5	2.719e+04	1.21e+01	4.757e−02	1.67e−03
HD015646	1	2.997e+03	4.84e+01	4.349e−02	1.36e−03
HD017254	5	4.622e+03	1.02e+01	4.368e−02	1.10e−03
HD019019	1	6.204e+03	3.74e+01	4.714e−02	1.41e−03
HD020722	1	5.818e+03	4.56e+01	3.517e−02	9.62e−04
HD020888	2	5.519e+03	2.04e+01	4.407e−02	1.19e−03
HD020902	1	6.872e+05	2.62e+03	4.361e−02	1.56e−03
HD021981	1	6.089e+03	1.33e+01	4.447e−02	1.22e−03
HD025860	1	4.202e+03	3.26e+01	4.031e−02	1.08e−03
HD027466	1	3.146e+03	3.18e+01	4.846e−02	1.46e−03
HD028099	1	2.546e+03	2.80e+01	4.635e−02	1.47e−03
HD028471	1	3.173e+03	1.81e+01	4.590e−02	1.39e−03
HD029461	1	2.759e+03	2.77e+01	4.736e−02	1.62e−03
HD030246	1	2.497e+03	2.75e+01	4.011e−02	1.38e−03
HD032831	1	2.301e+05	8.06e+02	4.509e−02	8.79e−04
HD034868	1	3.851e+03	3.89e+01	4.791e−02	1.46e−03
HD035666	1	3.416e+04	1.34e+02	4.578e−02	1.52e−03
HD036167	1	5.627e+05	2.23e+03	4.301e−02	2.54e−03
HD037962	1	3.281e+03	3.12e+01	4.565e−02	1.39e−03
HD038949	1	2.871e+03	3.10e+01	4.602e−02	1.51e−03
HD039608	6	3.861e+04	1.25e+01	4.455e−02	1.46e−03
HD040129	1	2.025e+03	2.04e+01	4.609e−02	1.43e−03
HD040335	1	2.866e+03	3.25e+01	4.383e−02	1.27e−03
HD041371	4	1.498e+04	1.16e+01	4.373e−02	1.00e−03
HD042525	1	5.116e+03	2.85e+01	4.460e−02	1.14e−03
HD042701	2	4.346e+04	1.20e+02	4.515e−02	8.27e−04
HD043107	14	8.368e+03	1.16e+01	4.660e−02	1.07e−03
HD044594	1	9.411e+03	4.79e+01	4.631e−02	1.30e−03
HD045557	1	5.492e+03	3.51e+01	4.228e−02	1.06e−03
HD046190	1	3.703e+03	2.82e+01	3.518e−02	9.61e−04
HD046819	1	8.504e+03	4.94e+01	4.627e−02	1.15e−03
HD047332	1	2.595e+03	2.60e+01	3.852e−02	1.05e−03
HD050310	1	7.865e+05	2.88e+03	5.228e−02	1.54e−03
HD053501	4	1.838e+05	3.71e+02	4.531e−02	1.03e−03
HD057336	1	1.403e+03	3.44e+01	4.446e−02	1.71e−03
HD058142	1	1.458e+04	1.33e+02	4.686e−02	2.57e−03
HD060178	1	2.584e+05	7.17e+02	4.808e−02	1.28e−03
HD061929	1	3.038e+03	2.66e+01	4.569e−02	1.35e−03
HD064324	1	3.672e+03	3.87e+01	4.256e−02	1.28e−03
HD065517	1	2.122e+03	1.81e+01	3.928e−02	1.19e−03
HD066751	1	9.671e+03	2.80e+01	4.704e−02	1.30e−03
HD069863	1	1.240e+04	5.52e+01	4.140e−02	9.15e−04
HD073210	1	3.707e+03	5.55e+01	4.261e−02	1.30e−03
HD073666	1	2.541e+03	5.66e+01	4.584e−02	1.59e−03
HD073819	1	3.170e+03	5.29e+01	4.553e−02	1.41e−03
HD077281	1	1.673e+03	1.99e+01	4.374e−02	1.30e−03
HD080007	2	2.594e+05	6.64e+02	4.536e−02	1.33e−03
HD082308	1	7.022e+05	2.59e+03	4.484e−02	1.32e−03
HD082621	1	1.909e+04	8.24e+01	4.679e−02	2.47e−03
HD087901	1	2.350e+05	7.87e+02	4.929e−02	1.39e−03
HD091375	1	1.602e+04	6.73e+01	4.646e−02	2.18e−03
HD092788	1	5.299e+03	3.93e+01	4.713e−02	1.64e−03
HD092845	1	7.166e+03	4.51e+01	3.975e−02	1.08e−03
HD096833	2	7.426e+05	2.07e+03	4.910e−02	1.26e−03
HD098230	1	1.467e+05	4.65e+02	4.635e−02	1.78e−03
HD098553	1	3.858e+03	3.39e+01	4.732e−02	1.41e−03
HD100167	1	5.036e+03	3.57e+01	4.587e−02	1.36e−03
HD101452	1	1.910e+03	3.50e+01	4.292e−02	1.45e−03
HD101472	1	3.834e+03	3.44e+01	4.534e−02	1.41e−03
HD101959	1	5.822e+03	3.20e+01	4.755e−02	1.38e−03
HD102647	2	2.365e+05	5.09e+02	3.519e−02	1.08e−03
HD102870	1	1.309e+05	5.02e+02	4.834e−02	3.18e−03
HD105805	1	5.734e+03	5.10e+01	4.692e−02	1.52e−03
HD106252	1	4.749e+03	3.73e+01	4.326e−02	1.35e−03
HD106965	1	1.248e+03	1.87e+01	4.533e−02	1.43e−03

TABLE 6 — *Continued*

Name	number of measurements	24μm count rate[a] (DN/s)	uncertainty (DN/s)	calibration factor (MJy/sr/[DN/s])	uncertainty (MJy/sr/[DN/s])
HD108799	1	1.242e+04	4.16e+01	4.490e−02	1.28e−03
HD108944	1	4.431e+03	3.10e+01	4.443e−02	1.25e−03
HD109612	1	1.260e+04	6.56e+01	3.864e−02	1.04e−03
HD109866	1	4.368e+03	2.77e+01	9.297e−02	2.62e−03
HD110304	1	1.510e+05	5.70e+02	4.672e−02	1.20e−03
HD112196	1	6.345e+03	3.41e+01	4.660e−02	1.39e−03
HD115043	1	7.863e+03	3.29e+01	4.500e−02	1.26e−03
HD115780	2	1.041e+04	9.28e+01	1.592e−02	4.59e−04
HD116706	1	6.188e+03	5.01e+01	4.846e−02	1.33e−03
HD119545	1	1.360e+05	2.33e+03	1.412e−03	4.37e−05
HD121370	1	3.132e+05	1.17e+03	4.878e−02	1.80e−03
HD121504	1	4.016e+03	4.34e+01	4.169e−02	2.27e−03
HD122652	1	5.100e+03	2.87e+01	4.378e−02	1.28e−03
HD123123	1	6.343e+05	2.39e+03	4.503e−02	1.20e−03
HD127665	1	6.687e+05	2.51e+03	4.545e−02	1.26e−03
HD128998	1	4.824e+03	2.79e+01	4.808e−02	1.22e−03
HD129655	1	2.577e+03	2.87e+01	3.807e−02	1.16e−03
HD131986	1	7.721e+03	9.91e+01	1.218e−02	3.69e−04
HD132417	1	5.041e+03	5.49e+01	2.860e−02	8.01e−04
HD132439	1	5.055e+03	3.77e+01	5.481e−02	1.50e−03
HD134493	1	2.956e+04	1.24e+02	4.625e−02	1.59e−03
HD138265	2	1.446e+05	4.23e+02	4.470e−02	1.12e−03
HD139698	1	8.006e+03	1.99e+02	9.042e−03	3.47e−04
HD141937	1	5.126e+03	3.82e+01	4.672e−02	1.34e−03
HD144873	1	1.723e+03	1.96e+01	4.887e−02	1.49e−03
HD150680	1	3.335e+05	1.33e+03	4.815e−02	1.86e−03
HD150706	1	6.656e+03	3.12e+01	4.339e−02	1.21e−03
HD152222	3	5.150e+04	1.92e+01	4.284e−02	1.79e−03
HD153458	1	2.799e+03	3.91e+01	4.584e−02	1.44e−03
HD154391	1	3.023e+04	1.22e+02	4.407e−02	1.16e−03
HD158460	1	7.931e+03	5.71e+01	3.748e−02	8.97e−04
HD158485	1	3.564e+03	2.80e+01	4.583e−02	1.27e−03
HD159048	1	3.600e+04	1.88e+02	4.359e−02	1.18e−03
HD159222	5	1.010e+04	1.02e+01	4.862e−02	1.25e−03
HD159330	102	7.929e+04	1.65e+01	4.525e−02	1.12e−03
HD163466	3	2.938e+03	1.90e+01	4.586e−02	1.19e−03
HD163588	2	4.479e+05	1.34e+03	4.604e−02	8.93e−04
HD165459	2	3.843e+03	2.48e+01	2.816e−02	9.77e−04
HD166780	2	3.065e+04	8.84e+01	4.505e−02	1.52e−03
HD167389	1	4.449e+03	2.66e+01	4.735e−02	1.35e−03
HD170693	4	1.855e+05	2.14e+01	4.638e−02	1.04e−03
HD172066	1	3.368e+03	2.68e+01	4.486e−02	1.31e−03
HD172728	2	4.747e+03	2.21e+01	4.980e−02	1.24e−03
HD173398	46	3.031e+04	1.84e+01	4.590e−02	1.54e−03
HD173511	1	3.165e+04	1.24e+02	4.485e−02	1.19e−03
HD173976	1	4.749e+04	1.72e+02	4.371e−02	1.10e−03
HD174123	1	2.296e+03	2.39e+01	4.936e−02	1.48e−03
HD176841	1	3.644e+03	2.79e+01	4.776e−02	1.43e−03
HD180711	2	5.759e+05	1.47e+03	4.529e−02	8.76e−04
HD183439	2	7.200e+05	2.64e+03	4.631e−02	1.67e−03
HD189276	2	3.857e+05	1.02e+03	4.392e−02	1.28e−03
HD191854	3	4.867e+03	1.97e+01	4.788e−02	1.41e−03
HD193017	1	4.150e+03	3.86e+01	4.956e−02	1.45e−03
HD195034	1	6.127e+03	3.33e+01	4.837e−02	1.49e−03
HD199598	1	7.021e+03	3.60e+01	4.637e−02	1.30e−03
HD201941	1	2.900e+03	2.79e+01	3.603e−02	1.04e−03
HD204277	1	7.301e+03	2.83e+01	4.606e−02	1.31e−03
HD205905	1	7.871e+03	3.42e+01	4.658e−02	1.41e−03
HD209952	2	1.465e+05	3.74e+02	4.542e−02	1.54e−03
HD212291	1	3.319e+03	3.19e+01	4.617e−02	1.55e−03
HD216131	1	3.277e+05	1.24e+03	4.440e−02	1.24e−03
HD216275	1	5.062e+03	4.07e+01	4.715e−02	1.39e−03
HD217382	1	3.264e+05	1.18e+03	4.375e−02	1.25e−03
NPM1+61.0569	1	1.510e+03	1.64e+01	4.481e−02	1.25e−03
NPM1+68.0412	1	1.494e+03	1.67e+01	4.700e−02	1.37e−03
SAO9310	1	1.069e+03	1.24e+01	5.655e−02	1.63e−03

[a] The count rates in this table can be converted to Jy by multiplying by the product of the aperture correction, calibration factor, and pixel area discussed in the text, or a factor of 6.92×10^{-6}.

TABLE 7
STARS REJECTED AS 24 μM CALIBRATORS.

Name	Reason for Rejection
BD+621644	calibration factor 12% low
HD011413	calibration factor 18% low[a]
HD020722	double source[b]
HD046190	calibration factor 29% low[c]
HD047332	calibration factor 18% low[a]
HD065517	calibration factor 16% low[a]
HD092845	double star
HD102647	calibration factor 29% low[c]
HD109612	bright, complex background
HD109866	bright, complex background
HD115780	bright, complex background
HD119545	bright, complex background
HD129655	calibration factor 19% low[a]
HD131986	bright, complex background and nearby contaminating sources
HD132417	bright, complex background and nearby contaminating sources
HD132439	bright, complex background
HD139698	bright, complex background
HD158460	calibration factor 21% low[c]
HD165459	calibration factor 61% low[c]
HD201941	calibration factor 26% low[d]
SAO9310	calibration factor 20% high

[a]NIR measurements indicate this star is reddened, so the predicted flux is likely low.

[b]There is a 24μm source 14$''$ to the north of this star. SIMBAD does not indicate the star is part of a multiple system and the *Spitzer* Planning and Observation Tool (SPOT) does not indicate any asteroids in the field, so the source is likely a background galaxy.

[c]Su et al. (2006) find this source has a debris disk.

[d]This star is not known to be part of a multiple system and no asteroids were expected in the field, so this star likely has an infrared excess.

TABLE 8
24 μM Observations of Cohen et al. Template Stars

	observed		template prediction			
Name	$f_\nu(24\mu\mathrm{m})$ (Jy)	unc. (Jy)	$f_\nu(24\mu\mathrm{m})$ (Jy)	unc. (Jy)	observed / template	unc.
HD032831	1.592e+00	5.58e−03	1.560e+00	5.99e−02	1.020	0.039
HD053501	1.271e+00	2.57e−03	1.238e+00	1.08e−01	1.027	0.089
HD163588	3.098e+00	9.27e−03	3.018e+00	1.06e−01	1.027	0.036
HD189276	2.668e+00	7.06e−03	2.559e+00	8.31e−02	1.043	0.034
HD138265	1.000e+00	2.93e−03	9.507e−01	3.25e−02	1.052	0.036
HD036167	3.893e+00	1.54e−02	3.800e+00	1.27e−01	1.024	0.035
HD170693	1.283e+00	1.48e−04	1.291e+00	4.57e−02	0.994	0.035
HD009927	4.182e+00	1.69e−02	3.908e+00	2.94e−01	1.070	0.081
HD134493	2.045e−01	8.58e−04	2.017e−01	6.90e−03	1.014	0.035

Note. — The star HD020722 has a template and was observed at 24 μm, but was not included in this comparison due to a nearby source at 24 μm (cf. Table 7).

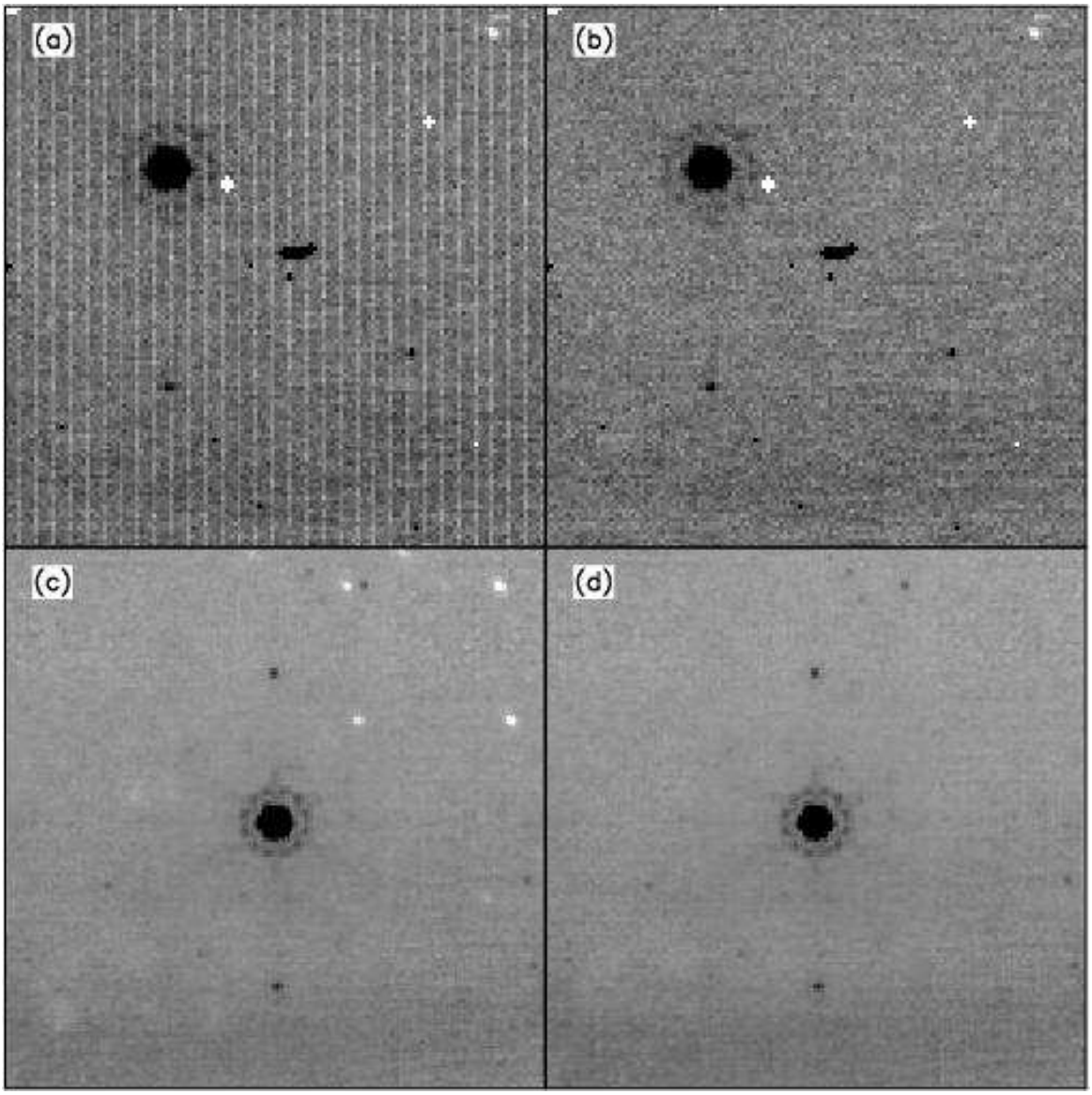

FIG. 1.— Artifacts not discussed by Gordon et al. (2005) that are now fixed as part of standard processing with the MIPS Data Analysis Tool (DAT), illustrated using observations of HD 159330 (AORKEY 13587712) plotted in reverse grayscale. (a) The "jailbar" effect is most easily seen in individual frames, here caused by a cosmic ray below and to the right of the star, and (b) fixed as described in § 2. (c) The spots caused by debris on the pick-off mirror (several sharp white spots above and to the right of the star, as well as diffuse white regions below and to the left of the star) are most easily seen in a mosaicked image and are (d) fixed using separate flat fields for each scan mirror position.

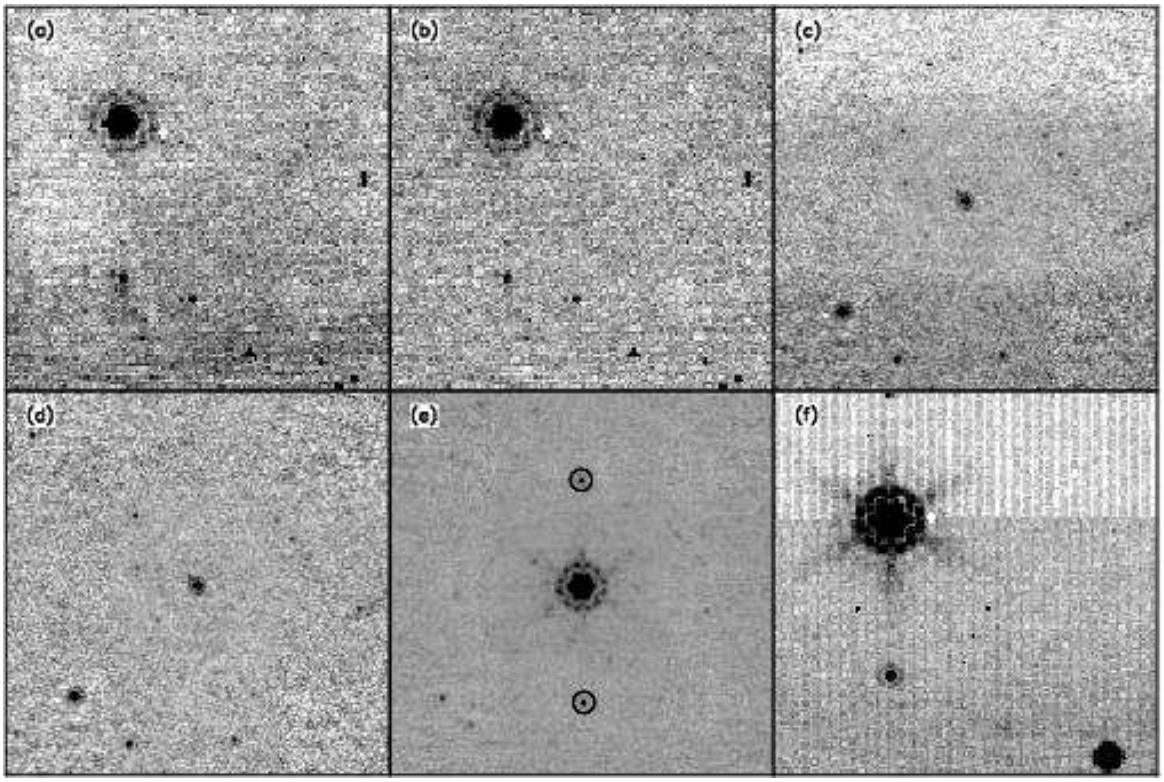

FIG. 2.— Artifacts not removed by standard processing with the MIPS Data Analysis Tool (DAT), plotted in reverse grayscale. As discussed in § 2, (a) gain changes imposed by previous observations (illustrated using a single-frame observation of HD 159330, AORKEY 12195328) are (b) removed using a second flat field. (c) Background changes as a function of scan mirror position (illustrated using a mosaic observation of HD 106965, AORKEY 13201920) are (d) removed before mosaicking. For the targets discussed here, the effects of (e) residual images (circled, illustrated using a mosaic observation of HD 159330, AORKEY 12195328) and (f) sources which saturate in 3 seconds (illustrated using a single-frame observation of HD 180711, AORKEY 9805568) are small and we make no correction.

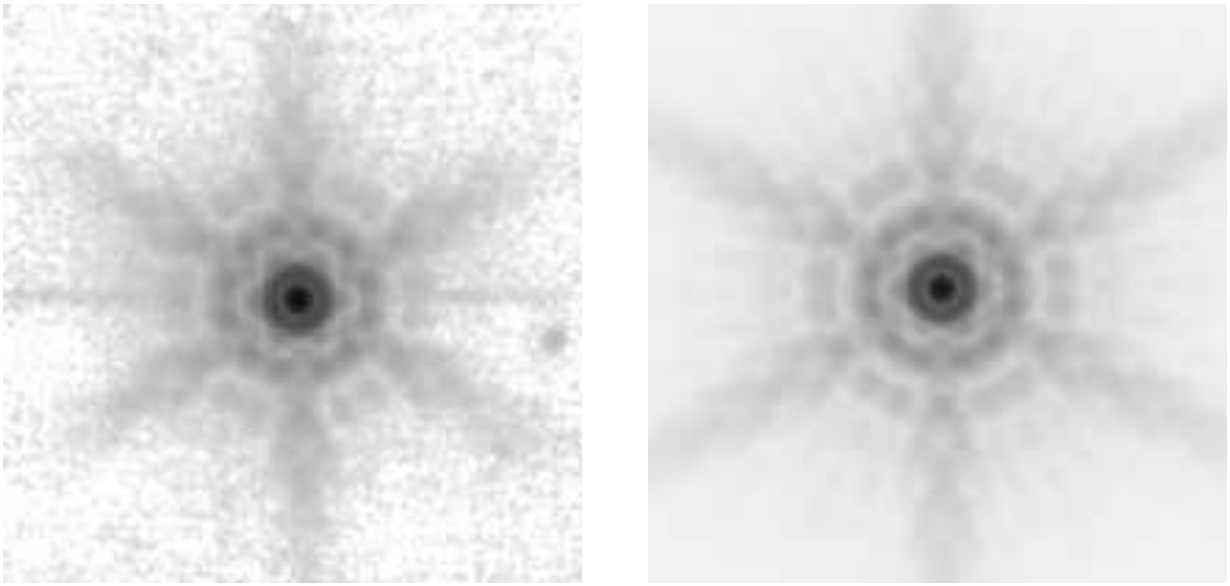

FIG. 3.— Comparison of observed and model PSF, plotted in reverse grayscale. On the left is shown an image of HD 009927; the horizontal feature through the center of the image is a detector artifact. The dynamic range (from the peak brightness of 60,000 DN/s to the 1σ noise level of 3 DN/s) is 20,000. The image on the right is a model generated by StinyTim, after processing through the MIPS simulator (see § 2.4). Both images have been heavily compressed using an asinh transform to show faint structure and the grayscale levels have been adjusted by eye to match each other.

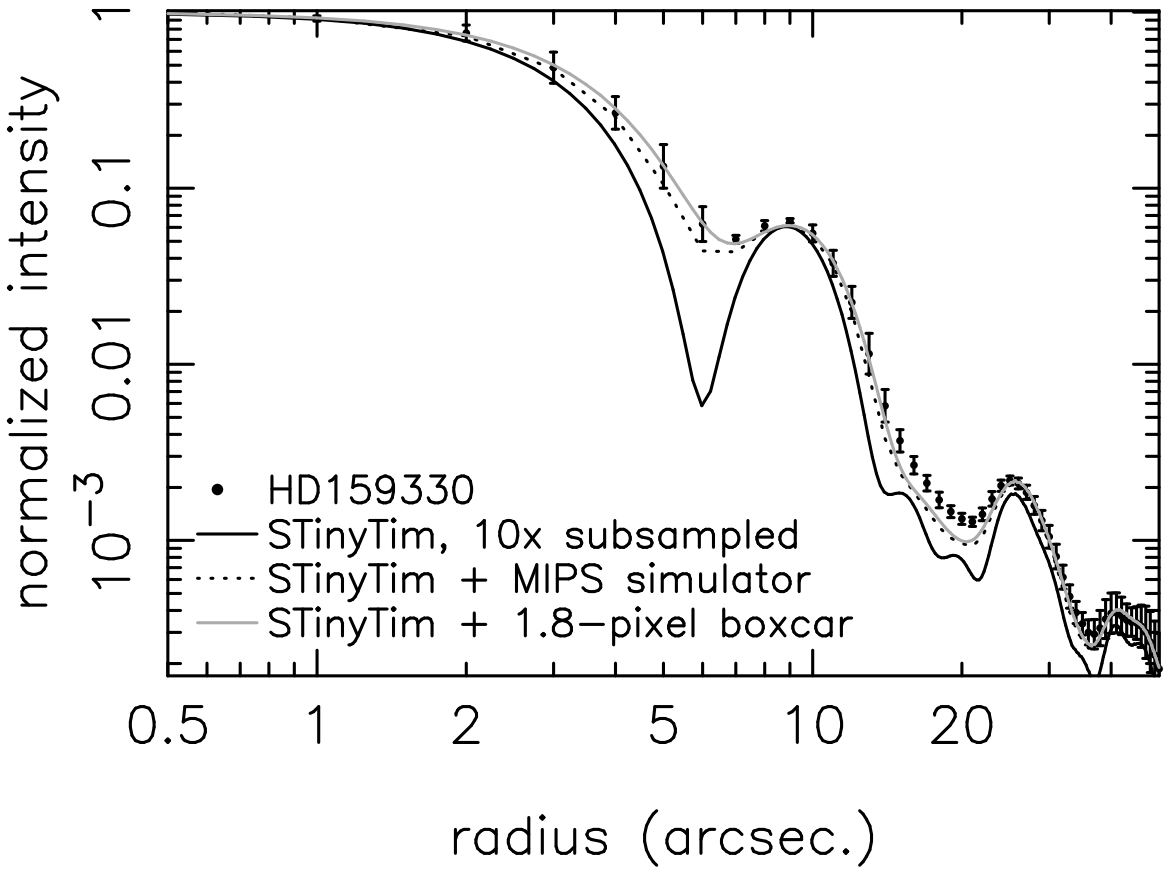

FIG. 4.— The radial profile of a star (points), compared to a 10× subsampled model profile generated by STinyTim (dark solid line), along with that same model profile run through the MIPS simulator (dark dotted line; see §2 for details) or smoothed by a 1.8-pixel boxcar (light solid line).

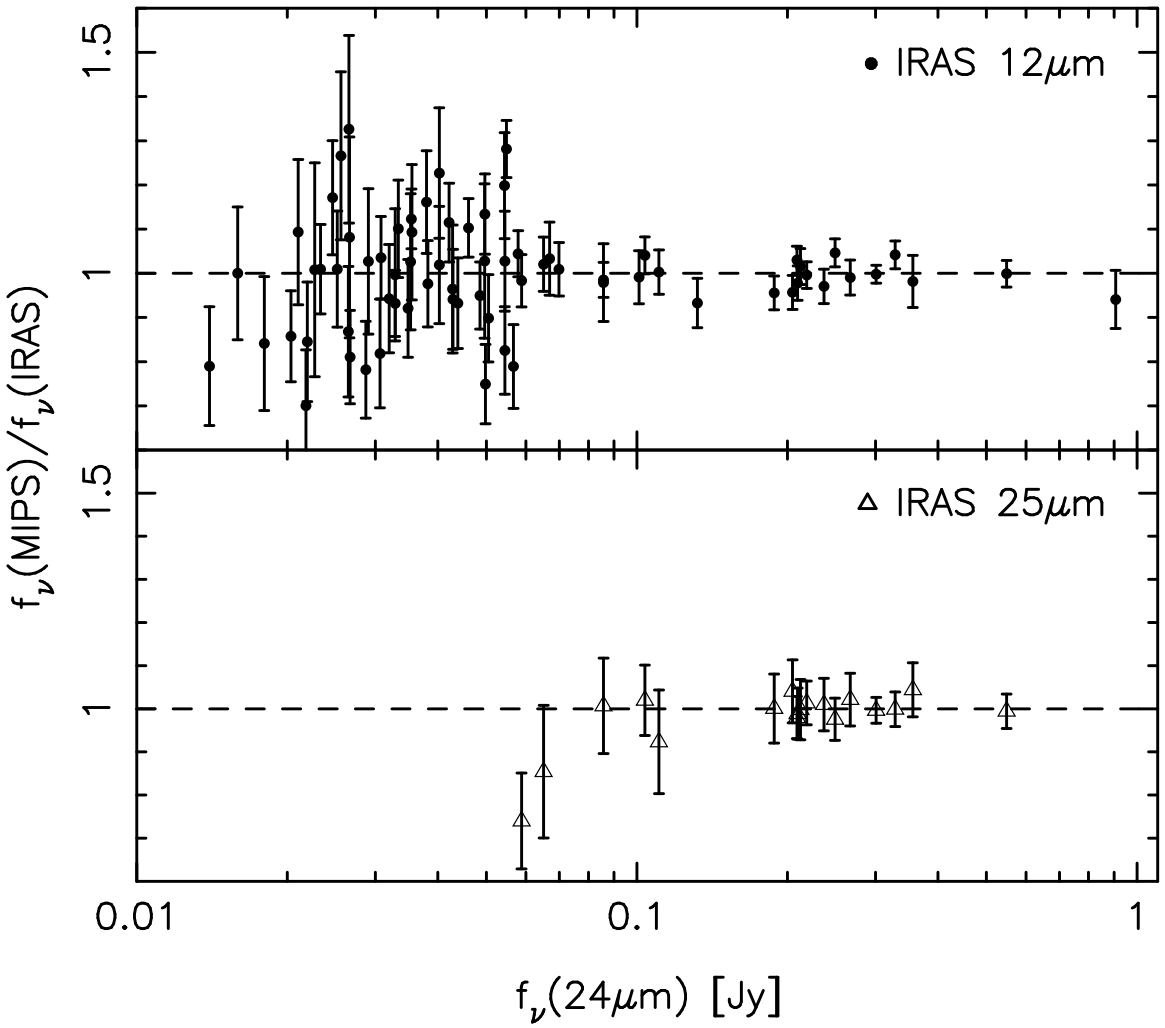

FIG. 5.— The ratio of MIPS 24 μm flux densities to IRAS 12 and 25 μm flux densities (filled circles and open triangles, respectively) as a function of 24 μm flux density, normalized to the average ratios of 0.265 and 1.11, respectively. The error bars represent the combined IRAS and MIPS uncertainties. A dashed line is drawn at a ratio of 1 as a guide.

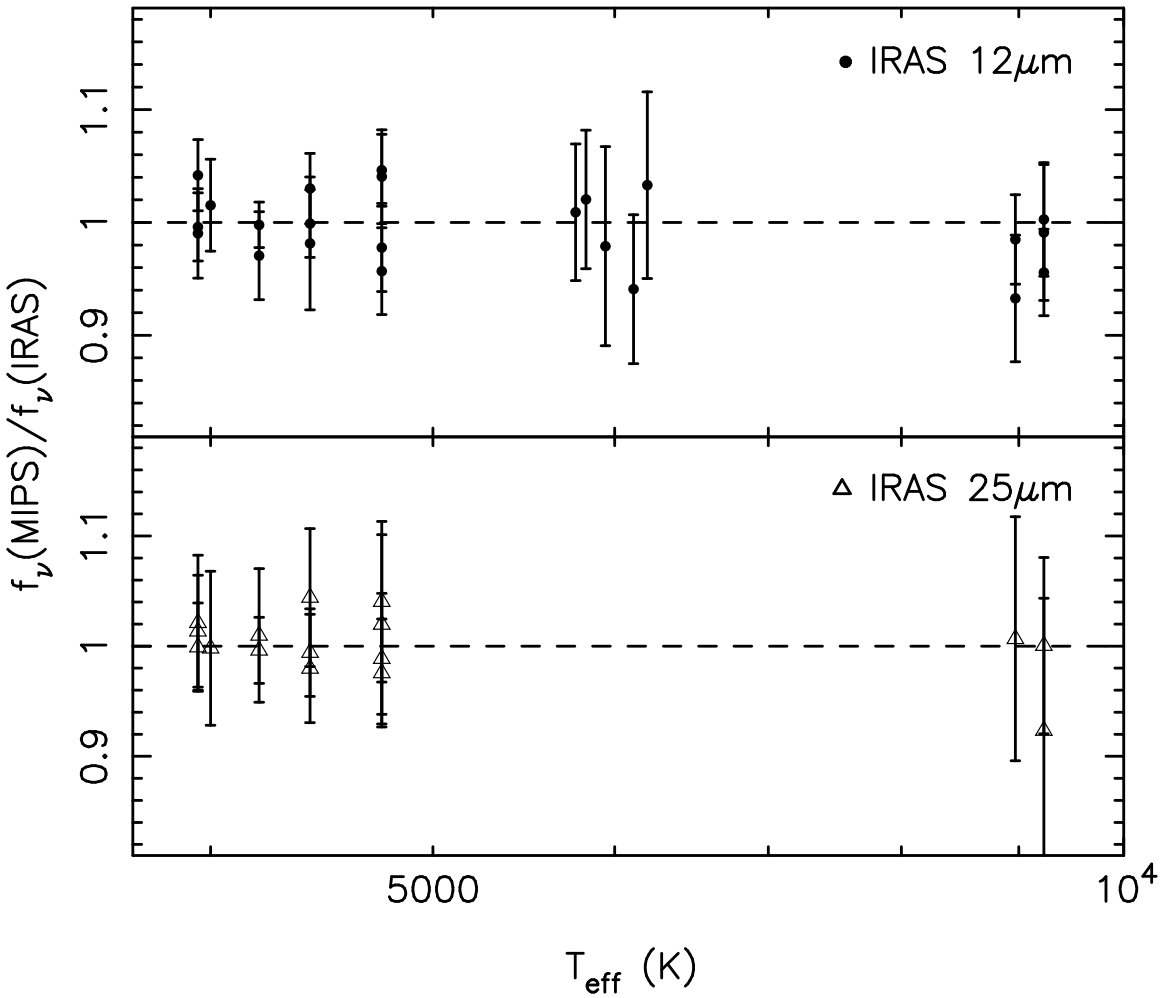

FIG. 6.— The ratio of MIPS 24 μm flux densities to IRAS 12 and 25 μm flux densities (filled circles and open triangles, respectively) as a function of spectral type, here quantified as the effective temperature of the star. The ratios have been normalized to the average ratios at 0.265 and 1.11 at 12 and 25 μm. The error bars represent the combined IRAS and MIPS uncertainties. A dashed line is drawn at a ratio of 1 as a guide.

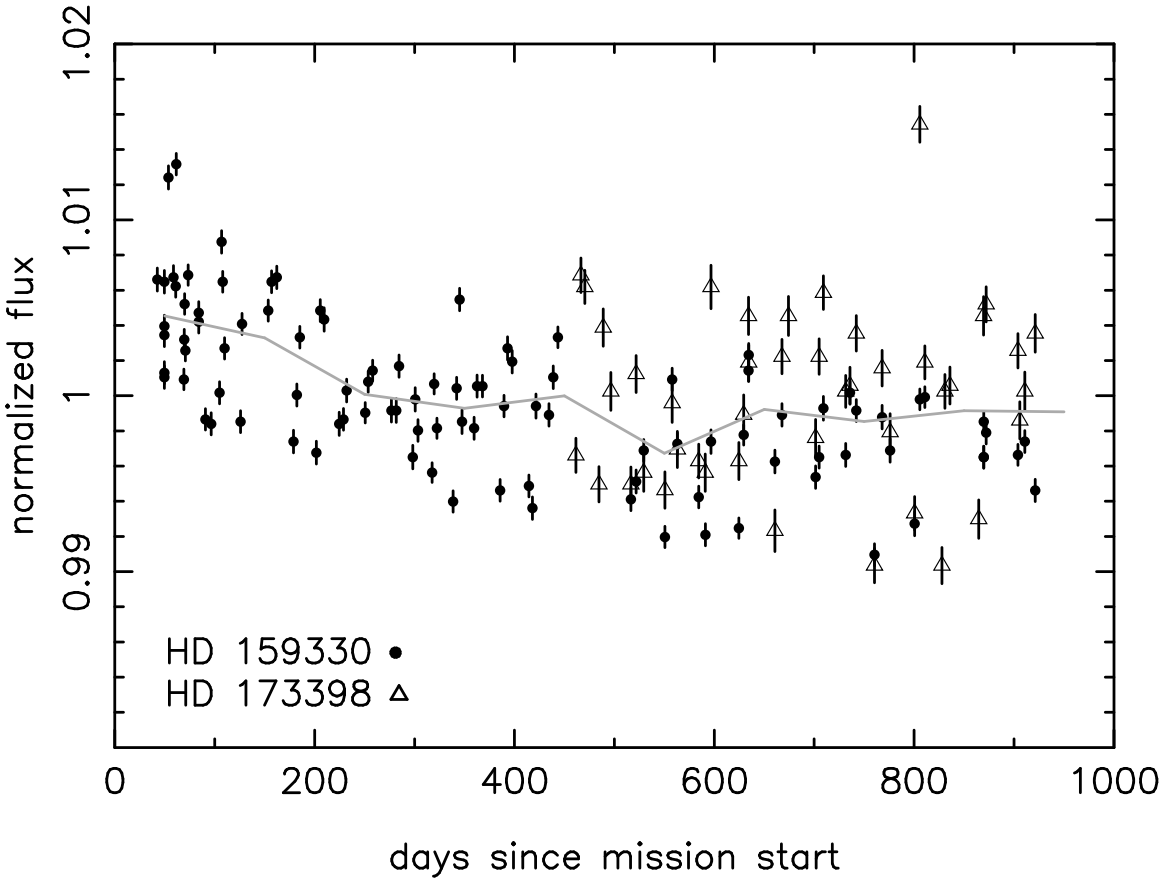

FIG. 7.— Repeatability of 24 μm photometry on two routinely-monitored sources: HD 159330 (filled circles) and HD 173398 (open triangles). The gray curve is a sigma-clipped average in 10 equally-spaced bins.

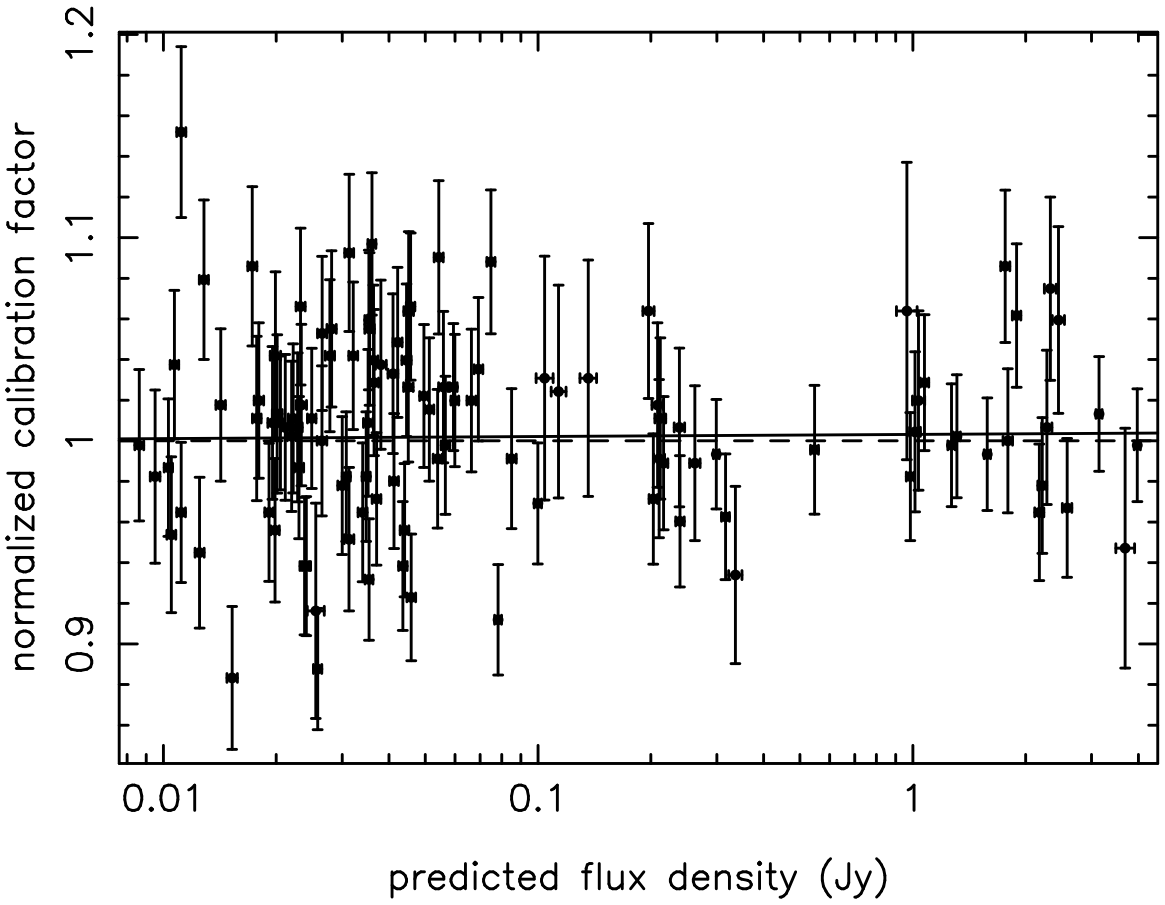

FIG. 8.— 24 μm calibration factor normalized to the nominal calibration factor (see § 3) as a function of predicted 24 μm flux density. The error bars are drawn from Tables 5 and 6. The dashed line is drawn at 1 as a guide, while the solid line is a linear least-squares fit to the data (see § 5). Points greater than 5σ above or below the nominal calibration factor have been not been included in the plot or the fit.

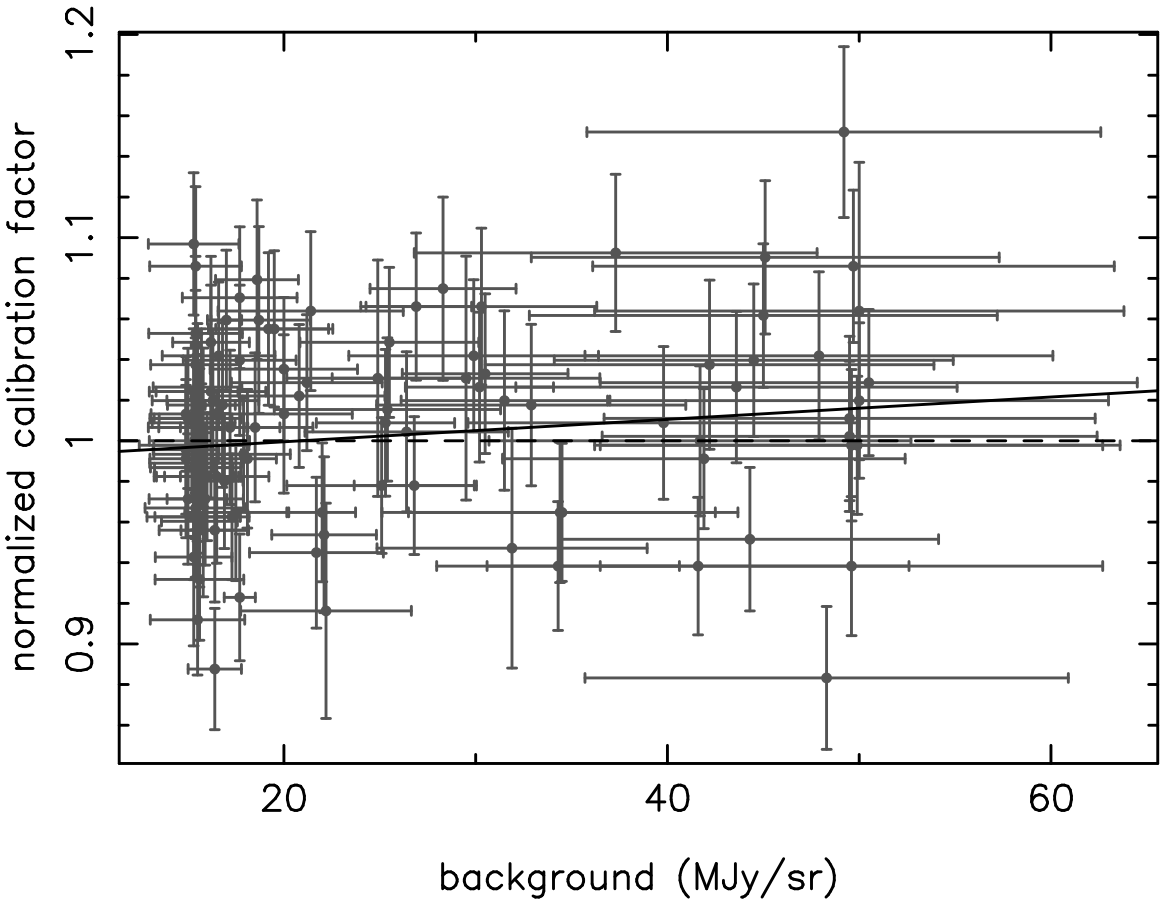

FIG. 9.— 24 μm calibration factor normalized to the nominal calibration factor (see § 3) as a function of predicted background. The uncertainties represented by the error bars are drawn from Tables 5 and 6. The dashed line is drawn at 1 as a guide, while the solid line represents a linear least-squares fit to the data (see § 5). Points greater than 5σ above or below the nominal calibration factor have been not been included in the plot or the fit.

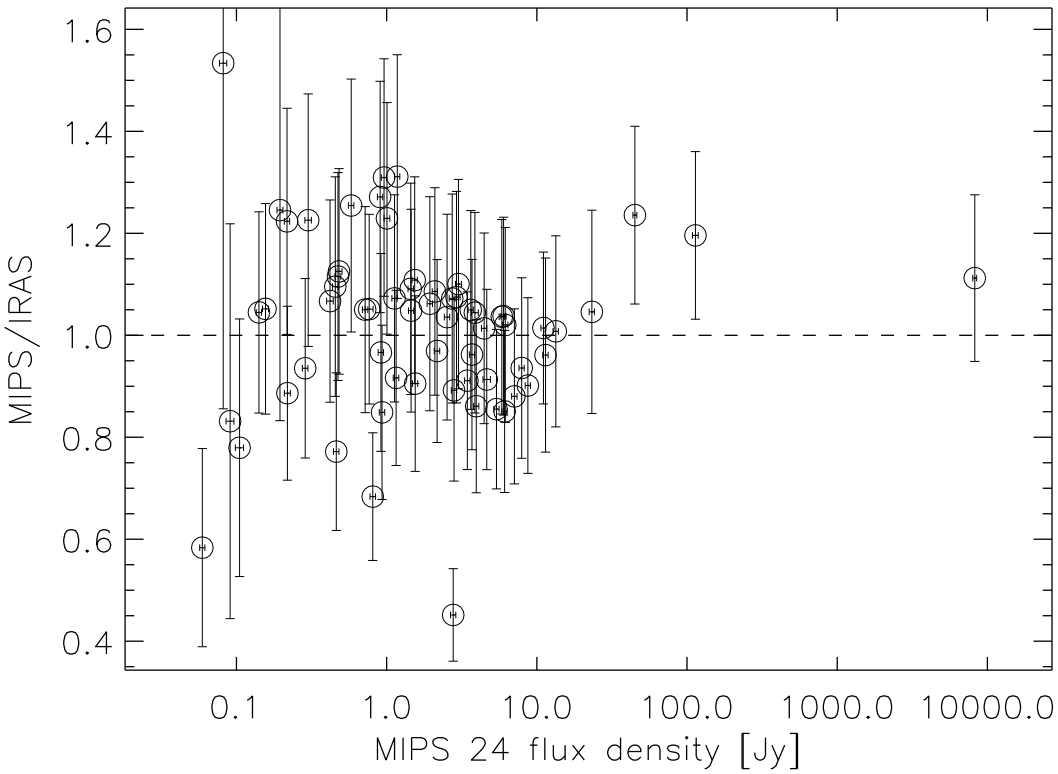

FIG. 10.— Ratio of MIPS to IRAS measurements of extended sources as a function of flux density measured at 24 μm. The error bars represent the combined uncertainty on both measurements. The dashed line is drawn at 1 as a guide.